

LIFE SCIENCES

Metabolic rewiring caused by mitochondrial dysfunction promotes mTORC1-dependent skeletal aging

Kristina Bubb¹, Julia Etich¹, Kristina Probst¹, Tanvi Parashar¹, Maximilian Schuetter², Frederik Dethloff², Susanna Reincke¹, Janica L. Nolte^{3,4}, Marcus Krüger^{3,4}, Ursula Schlötzer-Schrehard⁵, Julian Nüchel⁶, Constantinos Demetriades^{6,4}, Patrick Gialvalisco², Jan Riemer^{4,7}, Bent Brachvogel^{1,4,8,*}

Decline of mitochondrial respiratory chain (mtRC) capacity is a hallmark of mitochondrial diseases. Patients with mtRC dysfunction often present reduced skeletal growth as a sign of premature cartilage degeneration and aging, but how metabolic adaptations contribute to this phenotype is poorly understood. Here we show that, in mice with impaired mtRC in cartilage, reductive/reverse TCA cycle segments are activated to produce metabolite-derived amino acids and stimulate biosynthesis processes by mechanistic target of rapamycin complex 1 (mTORC1) activation during a period of massive skeletal growth and biomass production. However, chronic hyperactivation of mTORC1 suppresses autophagy-mediated organelle recycling and disturbs extracellular matrix secretion to trigger chondrocytes death, which is ameliorated by targeting the reductive metabolism. These findings explain how a primarily beneficial metabolic adaptation response required to counterbalance the loss of mtRC function, eventually translates into profound cell death and cartilage tissue degeneration. The knowledge of these dysregulated key nutrient signaling pathways can be used to target skeletal aging in mitochondrial disease.

INTRODUCTION

Mitochondrial diseases are rare genetic disorders causing a decline of the mitochondrial respiratory chain (mtRC) function (1, 2). Originally, clinical phenotypes in mitochondrial diseases were described to arise mainly from energy depletion due to impaired mtRC function, but this concept neglected the importance of mitochondria for biosynthetic processes. Mitochondria produce metabolic precursors required for protein, lipid and nucleotide synthesis, as well as for extracellular matrix (ECM) production. Recent cohort studies showed that energy-consuming metabolic pathways become activated in patients with mitochondrial disease associated with perturbations in protein secretion, faster cellular aging, and skeletal growth retardation (3–5). Despite these findings, the precise molecular implications remain largely uncertain.

Skeletal growth is driven by the epiphyseal growth plate cartilage, a remarkable tissue that generates a high amount of biomass under metabolic challenging conditions. The avascular hypoxic growth plate relies mainly on glycolysis during early development but activates mitochondrial respiration later after birth (6). The metabolic switch is required to sustain the proliferation and differentiation of chondrocytes and secrete a large quantity of specialized ECM material for structural support in a postnatal period of massive skeletal

growth. Later, during adolescence in humans, transient growth plate cartilage is resorbed and replaced by bone. This process known as age-dependent growth plate fusion leads to physiological skeletal growth arrest in humans. In contrast, growth plates are often maintained throughout life in mice (7). We could recently show that the loss of mtRC function provokes growth plate fusion and growth retardation in elderly mutant mice with a cartilage-specific deletion of mitochondrial DNA (mtDNA) (6, 8). Therefore, this mouse model of mitochondrial dysfunction mimics a skeletal aging situation in humans and allows us to now define the molecular basis of the physiological aging response in growth plate cartilage with mitochondrial dysfunction.

In the present study, we used these transgenic mice expressing a mutant mitochondrial helicase (Twinkle^{K320E}) driven by the Col2a1 promoter to inactivate mtDNA-encoded genes that are crucial for mtRC function. A previously conducted detailed molecular analysis revealed that these mice show mtDNA depletion, leading to a marked reduction in mitochondrial membrane potential, adenosine triphosphate (ATP) production, and reactive oxygen species levels, while simultaneously increasing lactate production. The metabolic alterations arise from the failure to switch from glycolysis to mitochondrial respiration in postnatal growth plate cartilage, as demonstrated by Seahorse experiments and in situ cytochrome c oxidase activity assays (6, 8). This now allows us to study the consequences of impaired mitochondrial respiration on postnatal metabolism and skeletal aging processes. Our results show that, when mtRC is dysfunctional, skeletal aging is accelerated, leading to premature transformation of growth plate cartilage into bony tissue. In-depth biochemical characterization demonstrate that chondrocytes of the growth plate use the reverse tricarboxylic acid (TCA) cycle to compensate for the loss of oxidative phosphorylation (OXPHOS)-driven metabolite production in a strong reductive environment and can stimulate amino acid biosynthesis pathways in vivo to persistently hyperactivate

¹Department of Pediatrics and Adolescent Medicine, Experimental Neonatology, Faculty of Medicine and University Hospital Cologne, University of Cologne, Cologne, Germany. ²Metabolic Core Facility, Max Planck Institute for Biology of Ageing, Cologne, Germany. ³Institute of Genetics, University of Cologne, Cologne, Germany. ⁴Cologne Excellence Cluster on Cellular Stress Responses in Aging-Associated Diseases (CECAD), University of Cologne, Cologne, Germany. ⁵Department of Ophthalmology, University Hospital Erlangen, Friedrich-Alexander-University of Erlangen-Nürnberg, Erlangen, Germany. ⁶Max Planck Institute for Biology of Ageing (MPI-AGE), Cologne, Germany. ⁷Institute of Biochemistry, Redox Biochemistry, University of Cologne, Cologne, Germany. ⁸Center for Molecular Medicine Cologne (CMMC), University of Cologne, Cologne, Germany.

*Corresponding author. Email: bent.brachvogel@uni-koeln.de

the mechanistic target of rapamycin complex 1 (mTORC1) during skeletal growth. In the long term, this hyperactivation disturbs autophagy-dependent ECM synthesis and secretion pathways *in vivo* causing chondrocyte death and accelerating skeletal aging. Overall, we provide here a molecular scenario for how the rewiring of biosynthetic pathways in cells with chronic mtRC dysfunction translates into hyperactive mTORC1-dependent signaling response that accelerates skeletal aging processes.

RESULTS

A skeletal aging response is induced in mice with mtRC dysfunction in cartilage

To define the *in vivo* impact of chronic mtRC dysfunction on skeletal aging processes, we monitored the progress of age-related growth plate cartilage degeneration in femur heads of transgenic CreTW mice with a chondrocyte-specific mtDNA deletion (Fig. 1A). The loss of femur head cartilage transparency and increase in red color are indicative of age-related growth plate cartilage degeneration and secondary bone formation associated with expansion of the subchondral vasculature network (Fig. 1B). First signs of aging are already apparent at 3 months in CreTW mice compared to 6 months in Cre mice indicating that the aging process is strongly accelerated in CreTW mice. Histomorphological analysis confirmed accelerated cartilage degeneration (loss of orange cartilage-specific safranin O staining) and its replacement with bony tissue (unstained) over time in CreTW mice (Fig. 1C, arrows). Cartilage is fully replaced by bone after 4 months but still intact in Cre control. Hence, femur head cartilage ages prematurely when the mtRC is dysfunctional *in vivo*.

TCA cycle enzyme and metabolite levels are elevated

Presumably, mtRC dysfunction causes alterations in the cellular metabolism, which can contribute to the accelerated aging response *in vivo*. We then studied the metabolic consequences of chondrocyte-specific mtDNA deletion/depletion in transgenic CreTW mice and determined the relative levels of glycolysis and TCA-cycle metabolites (Fig. 2A) in femur head cartilage of 1-month-old mice using liquid chromatography–mass spectrometry (LC-MS)–based analysis. At this age, morphological differences between Cre and CreTW femora were already detected and still sufficient amounts of cartilage could be isolated for LC-MS–based analysis. Notably, lactate and other glycolytic metabolites like fructose-6-phosphate and pyruvate (Fig. 2B) were increased *in vivo* in femur head cartilage of CreTW mice compared to Cre control. In addition, levels of TCA cycle intermediates were elevated (Fig. 2C). These changes were accompanied by an increase in most enzymes (12 enzymes) of the TCA cycle and a decrease in abundance of several other proteins (43 entities) involved in mitochondrial OXPHOS (Fig. 2D) as determined by proteome analysis (8) of femur head cartilage. Notably, we also detected a reductive microenvironment with a decreased oxidized form of nicotinamide adenine dinucleotide (NAD⁺)/reduced form of NAD⁺ (NADH) ratio in CreTW cartilage (Fig. 2E), which is likely a consequence of impaired electron transfer from NADH to oxygen due to a defective mtRC. This characterization of the *in vivo* metabolic situation illustrates that chondrocyte-specific mtRC dysfunction activates glycolysis and, unexpectedly, increases TCA cycle–derived metabolite levels in femur head cartilage.

TCA cycle activity is reversed to replenish metabolite loss

mtRC activity is tightly connected with the TCA cycle, and we hypothesized that the loss of mtRC function redirects the passage of metabolites through glycolysis and the TCA cycle in chondrocytes. Hence, we used ¹³C₆ glucose feeding experiments to trace the metabolic fate of glucose-derived carbons in chondrocytes from 1-month-old Cre and CreTW mice. Chondrocytes were traced with ¹³C₆ glucose for 2 hours followed by LC-MS–based analysis. This time point captures an equilibrium time point in chondrocytes, where metabolite concentrations and enrichments remain relatively stable (fig. S3). Characterization of the ¹³C-enriched carbon (Fig. 3A, blue) revealed a small, but significant increase of m+6 label for glucose-6-phosphate (Glu-6-P) and fructose-1,6-bisphosphate (Fru-1,6-bP), along with an increase of m+3 label for 3-phosphoglycerate (3-PG), phosphoenolpyruvate (PEP), and lactate in chondrocytes from CreTW compared to control (Fig. 3B). The results confirmed the stimulation of glycolytic processes in CreTW chondrocytes to compensate for the loss of OXPHOS-dependent energy production and NAD⁺ regeneration. We then determined the ¹³C enrichment pattern of labeled carbon in the metabolites of the TCA cycle. Here, m+2 labels (clockwise/oxidative direction of the TCA cycle) for citrate, malate, fumarate, and succinate were significantly decreased, while m+3 labels of malate, fumarate, and succinate (reductive/counterclockwise anaplerotic entry of pyruvate into the TCA cycle) were significantly increased in CreTW chondrocytes compared to control (Fig. 3C fig. S3, B and D). Therefore, these labeling data indicate a pyruvate carboxylase–dependent pyruvate influx into oxaloacetate and a reverse (counterclockwise) activation of the TCA cycle segment from oxaloacetate to succinate. Similar molecular phenotypes have previously been described to occur when oxidative TCA cycle activity is blocked, leading to extreme reducing conditions (9). This is in line with the detection of higher NADH levels and a decrease of the NAD⁺/NADH ratio *in vivo* in cartilage with defective mtRC (see Fig. 1G) (6). Hence, glucose-derived carbon atoms are fed into the TCA cycle to stimulate this reverse segment and replenish metabolites like oxaloacetate and fumarate, required for amino acid and nucleotide biosynthesis to support cartilage-driven skeletal growth when mtRC is dysfunctional.

The glutamine-dependent reverse carbon enrichment from α -ketoglutarate to citrate can further support metabolite replenishment in reductive situations when mtRC is impaired (10). To understand the consequences for the activation of this second reverse segment, ¹³C₅ glutamine was fed to the chondrocytes and the incorporation of glutamine-derived carbons into the TCA cycle metabolites was measured (Fig. 3A, green). Here, an increase in the m+5 pattern of α -ketoglutarate, isocitrate, aconitate, and citrate was detected (Fig. 3D), indicating a glutamine-dependent reductive/counterclockwise carbon enrichment into this segment of the TCA cycle from α -ketoglutarate to citrate in cartilage with impaired mtRC function. In conclusion, our combined metabolic tracing analysis demonstrates the engagement of glycolytic pathways and the activation of two reverse segments of the TCA cycle to replenish metabolites required for biosynthetic reactions when mtRC is dysfunctional in cartilage.

Reverse TCA cycle activity stimulates amino acid–related pathways

Amino acids are among the direct products of TCA cycle–derived metabolites; we therefore studied their *de novo* biosynthesis in chondrocytes with defective mtRC function. Here, the combined metabolite studies detected an increased carbon enrichment into glycine,

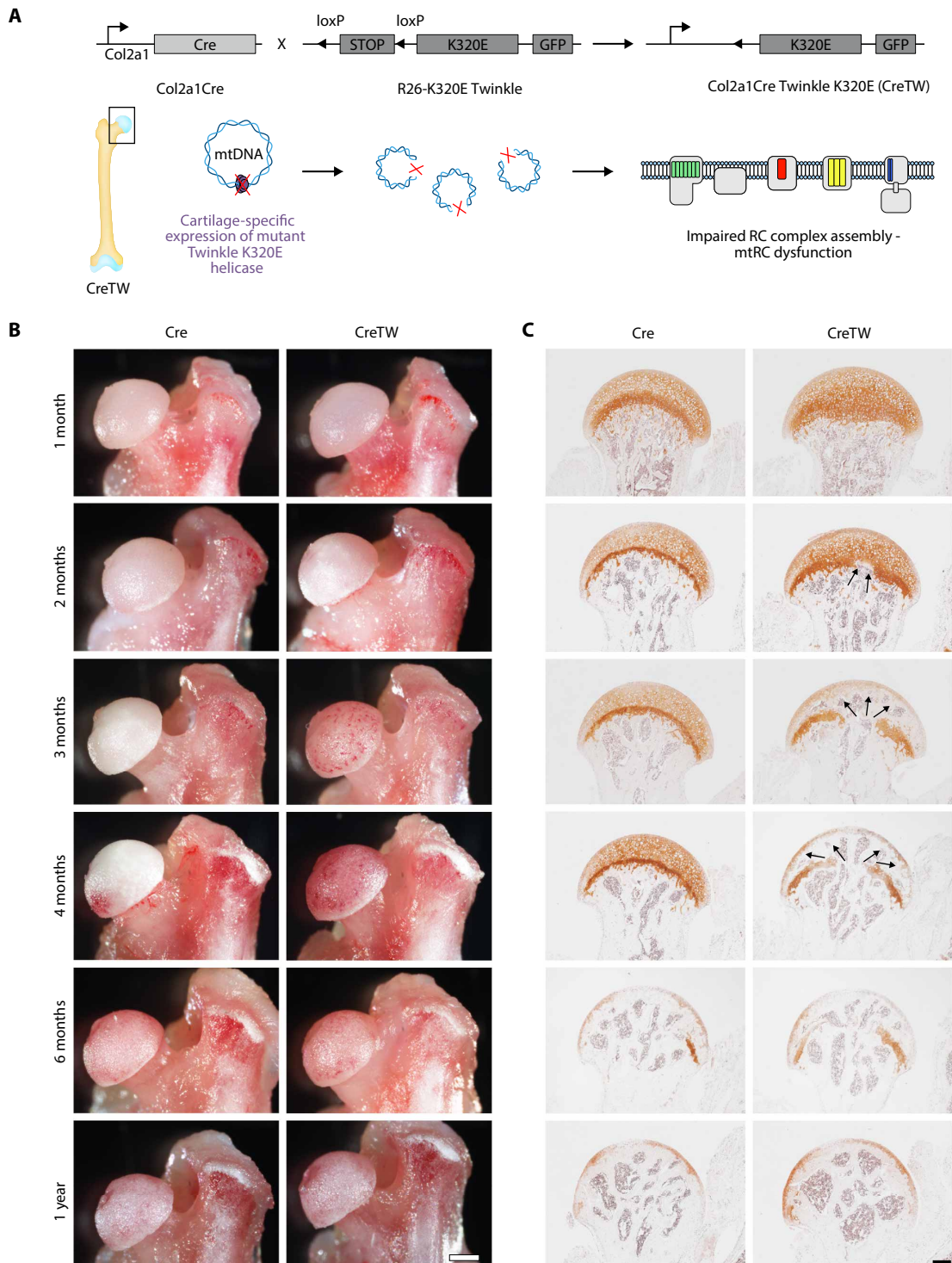


Fig. 1. Skeletal aging processes are accelerated in mutant mice with a defective mtRC in chondrocytes. (A) Breeding scheme: Generation of mice with a cartilage-specific expression of Twinkle^{K320E} mutant helicase (CreTW) (27). Consequences of Twinkle mutant expression for mitochondrial (mt) DNA and respiration complexes are illustrated. (B) Overview of the femur head morphology during aging in Cre and CreTW mice. The loss of transparency and the increase in red color shows age-related cartilage degeneration and secondary bone formation. (C) Histomorphological analysis of safranin O-stained femur head sections. Total femur head (orange) and growth plate cartilage (dark orange) are visualized. Arrows illustrate initiation sites of growth plate cartilage degeneration and its replacement with bony tissue (unstained). Scale bars, 500 μ m (B) and 100 μ m (C).

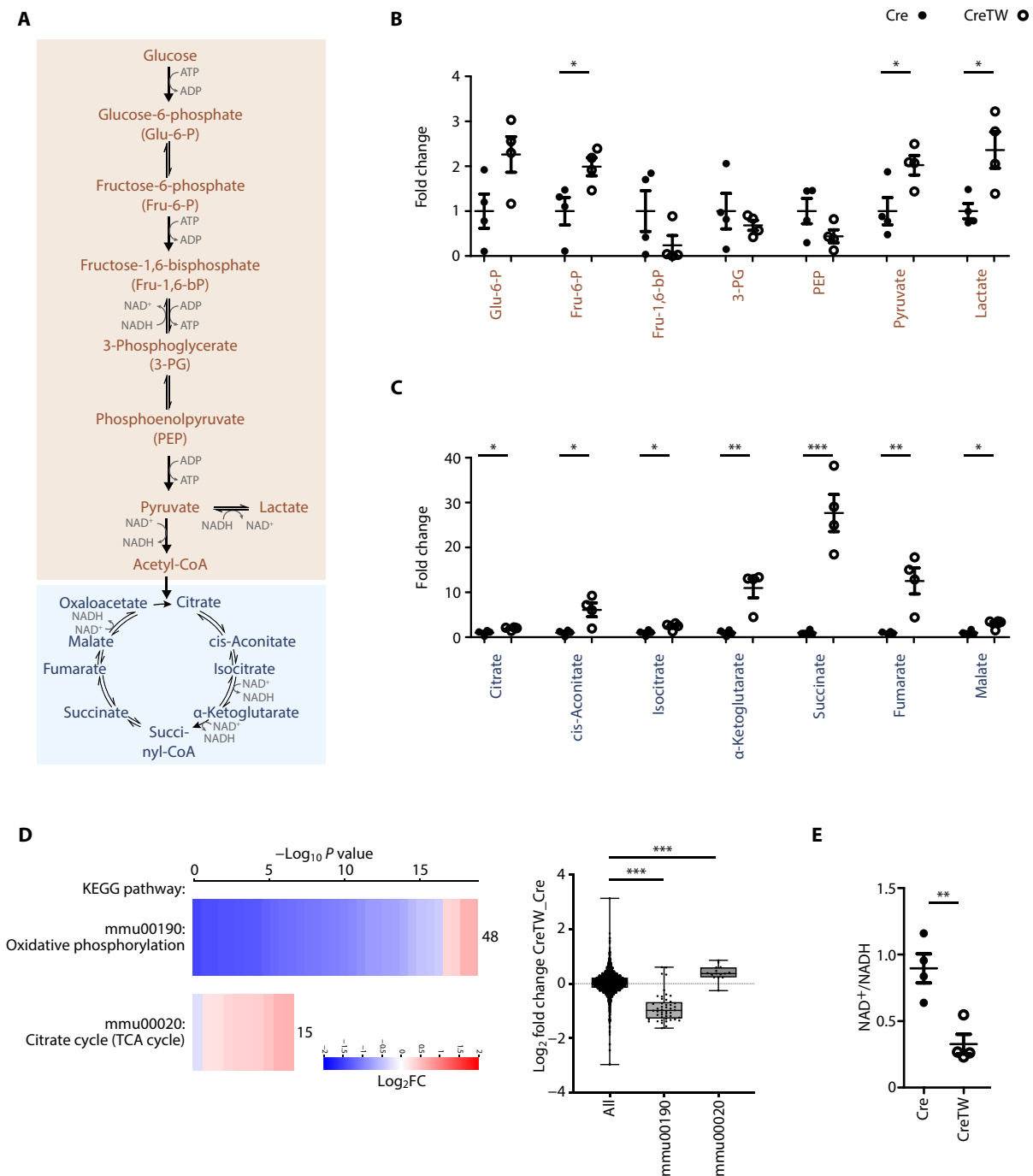


Fig. 2. Glycolysis is activated, and TCA cycle metabolites accumulate in vivo in cartilage with a defective mtRC. (A) Scheme of glycolysis and TCA cycle. (B) Glycolytic and (C) TCA cycle–derived metabolites in femur head tissue extracts of 1-month-old Cre and CreTW mice were quantified using LC-MS–based analysis. Raw data for peak values are provided in fig. S1. (D) Visualization of differentially abundant entities within the KEGG pathways “TCA cycle” and “OXPHOS” of CreTW mice using a proteome dataset generated from femur head tissue extracts of 1-month-old Cre and CreTW mice [PXD027109 and (8)]. The number of color-coded regulated entities within each pathway is shown, with the corresponding log₂ fold changes summarized in box plot to the right. Raw data for log₂ LFQ are provided in fig. S2. (E) NAD⁺/NADH ratio determined in femur head extracts from 1-month-old Cre and CreTW mice using colorimetric quantification assays (*n* = 4 animals per genotype). Data presented as means ± SEM. Unpaired two-tailed Student’s *t* test, **P* < 0.05, ***P* < 0.01, ****P* < 0.001.

Downloaded from https://www.science.org on May 03, 2025

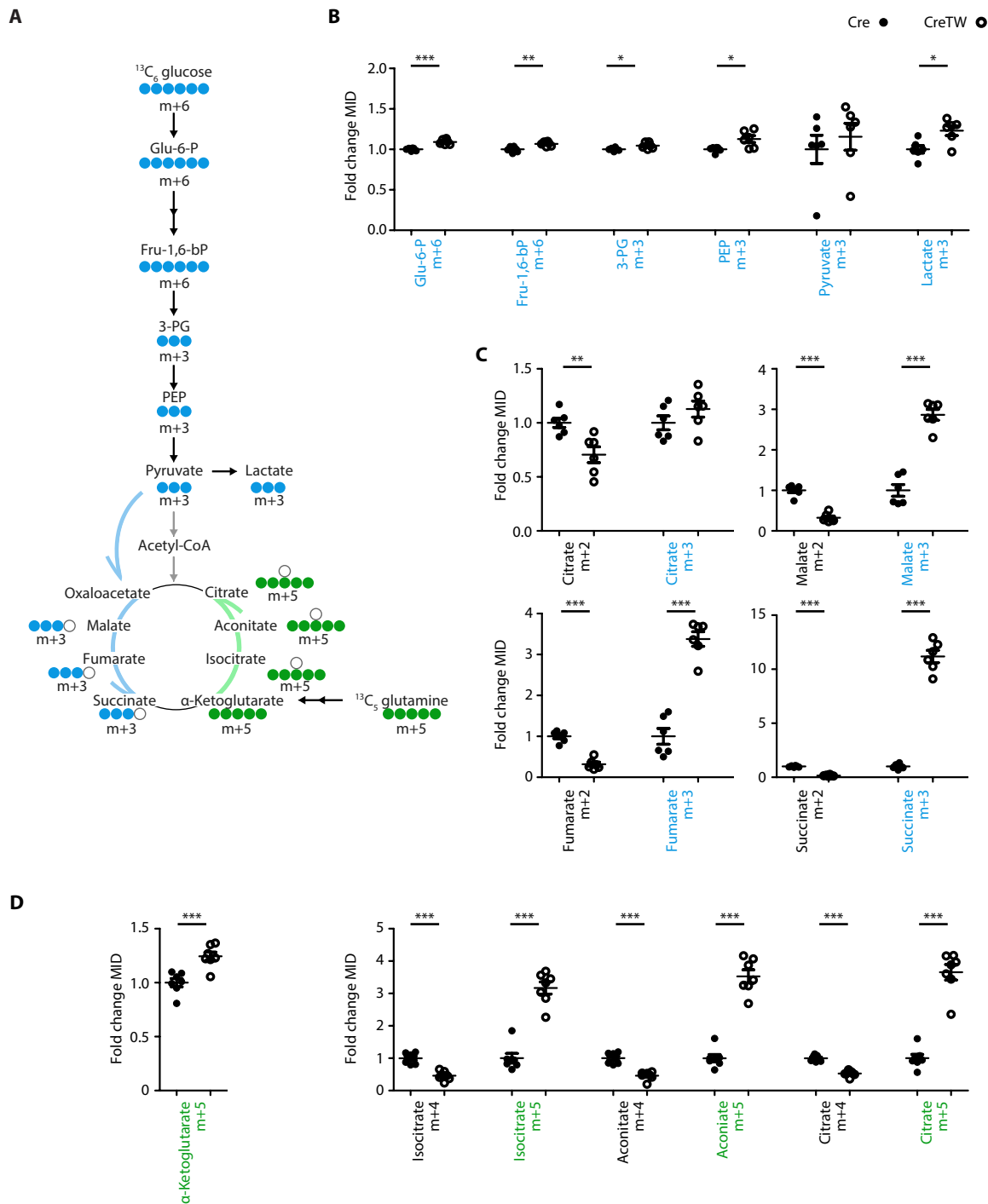


Fig. 3. Engagement of the reverse TCA cycle segments in chondrocytes with impaired mtRC. (A) Overview of the $^{13}\text{C}_6$ glucose and $^{13}\text{C}_5$ glutamine enrichment analysis in isolated ribcage chondrocytes. Circles represent the carbon atoms in metabolites. Blue color indicates the presence of ^{13}C atom originating from $^{13}\text{C}_6$ glucose; green color originates from $^{13}\text{C}_5$ glutamine. (B to D) Incorporation of labeled metabolites derived from $^{13}\text{C}_6$ glucose (B) and (C) and from $^{13}\text{C}_5$ glutamine (D) were determined by LC-MS-based analysis. Relative fold changes of the mass isotopomer distribution (MID) between genotypes are shown ($n = 6$ animals per genotype [$^{13}\text{C}_6$ glucose, (B) and (C)], $n = 7$ animals per genotype [$^{13}\text{C}_5$ glutamine, (D)]). Raw data are provided in figs. S4 and S5. Quantitative data are means \pm SEM. Unpaired two-tailed Student's t test, * $P < 0.05$, ** $P < 0.01$, *** $P < 0.001$.

alanine, aspartate, and proline in CreTW chondrocytes compared to control (Fig. 4A and fig. S7, A and B). These carbon label experiments could only be done in isolated chondrocyte cultures, and, therefore, consequences of the rewired metabolism for amino acid biosynthesis were next validated in vivo by LC-MS-based analysis using femur head cartilage. Kyoto Encyclopedia of Genes and Genomes (KEGG) pathway enrichment analysis confirmed that entities of the “biosynthesis of amino acids” are among the most strongly enriched terms, along with the terms “oxidative phosphorylation,” “TCA cycle,” and “carbon metabolism” in the proteome data of femur head cartilage from 1-month-old CreTW mice (Fig. 4B). The levels of most proteins that are linked to “biosynthesis of amino acids” and interconversion were increased in CreTW mice compared to control. Among those, we identified enzymes predominantly involved in the synthesis of glycolysis- and TCA cycle-derived amino acids (Fig. 4C). More specifically, we found PHGDH, PSAT1, and PSPH enzymes that convert the glycolytic metabolite 3-PG via serine to glycine, while ALDH18a1 and PYCR1 catalyze proline biosynthesis reactions.

Furthermore, we analyzed the steady-state levels of 19 amino acids in vivo in femur head cartilage from 1-month-old Cre and CreTW mice by LC-MS-based analysis. Among those, the nonessential amino acids aspartate, glycine, and proline and the essential amino acids isoleucine, phenylalanine, and valine were significantly increased in abundance in CreTW femur head cartilage (Fig. 4D). These results suggest that TCA cycle metabolites enter amino acid biosynthesis pathways to generate a unique profile of amino acids in cartilage when the chondrocyte mtRC is dysfunctional in vivo presumably to sustain protein synthesis reactions required for skeletal growth (11).

Perturbations in amino acid levels promote mTORC1 signaling

To define signaling networks that detect and translate the increase in metabolites and amino acids into cellular responses, we studied the phosphoproteome in femur head cartilage from 1-month-old Cre and CreTW mice using mass spectrometry. Here, EasyPhos technology was applied to maximize yield, coverage, and reproducibility of phosphopeptide quantification (12). In total, 2487 phosphoproteins were detected in femur head cartilage and among those, 40 proteins with 59 differentially phosphorylated sites were identified (Fig. 5A). Most phosphorylation sites correspond to nonvalidated sites previously identified by high-throughput proteomic analyses (<https://phosphosite.org>). Among the 14 validated phosphorylation sites, 4 correspond to mTOR signaling pathway targets (Fig. 5B), including the insulin receptor substrate 1 (pIRS^{S302}) and the eukaryotic translation initiation factor 4E-binding protein 1 (p4E-BP1^{S65}, p4E-BP1^{T70}). Immunoblot analysis using femur head cartilage samples confirmed that the phosphorylation of the downstream mTORC1 targets ribosomal S6 kinase beta-1 (S6K1^{T389}) and eukaryotic translation initiation factor 4E-binding protein 1 (4E-BP1^{S65} and 4E-BP1^{T37/46}) was strongly elevated in CreTW mice compared to controls (Fig. 5, C and D) accompanied by slightly higher total levels. In addition, the phosphorylation of adenosine monophosphate (AMP)-activated protein kinase (AMPK) on threonine-172 that is known to function as a negative upstream mTORC1 regulator (13, 14) was reduced in femur head cartilage of CreTW mice compared to control.

The phosphoproteomic signature and immunoblot analysis of cartilage with perturbed mtRC suggested that the elevated amino

acid levels cause the activation of mTORC1; therefore, we studied the phosphorylation of mTORC1-specific downstream targets in response to amino acid starvation in cultured chondrocytes from 1-month-old Cre and CreTW mice using immunoblot analysis (Fig. 5, E and F). The removal of amino acids strongly reduced the phosphorylation of the mTORC1 substrates S6K1 and 4E-BP1 in Cre and CreTW chondrocytes. After 2 and 16 hours of amino acid depletion, phosphorylation of ribosomal S6 kinase 1 (S6K1^{T398}) decreased in Cre chondrocytes, whereas the decrease of p-S6K1 was significantly delayed in CreTW chondrocytes. Long-term amino acid depletion (16 hours) reduced total 4E-BP1 levels in both Cre and CreTW chondrocytes. However, a decrease in electrophoretic mobility of 4E-BP1 as a measure for increased phosphorylation [hyperphosphorylated β - & γ form, (15)] was detected in CreTW chondrocytes compared to Cre control as well as its persistent phosphorylation (p4E-BP1^{S65}). This indicates that both mTORC1 targets remain hyperphosphorylated in chondrocytes with mtRC dysfunction despite external amino acid removal. To further extend this analysis, we examined the amino acid-dependent association of mTOR with lysosomes, a critical requirement for sustaining mTORC1 signaling activity in cells (16). Here, we observed that mTOR preferentially localizes to LAMP2⁺ lysosomes in CreTW chondrocytes compared to controls, both under standard growth conditions and after amino acid depletion (fig. S7, C and D).

We hypothesized that the increased amino acid biosynthesis activity in CreTW chondrocytes contributes to elevated intracellular levels of amino acids, which in turn sustain the phosphorylation of downstream mTOR kinase target proteins. We therefore analyzed the impact of the endogenously elevated amino acids [aspartate (D), phenylalanine (F), glycine (G), isoleucine (I), proline (P) and valine (V)] on mTORC1 activity. Chondrogenic cells were cultured for 2 hours in amino acid-depleted media and then stimulated for 2 hours with medium containing individual amino acids or medium supplemented with a mix containing all amino acids (Fig. 5, G and H). Immunoblot analysis revealed that phosphorylation of S6K1 and 4E-BP1 was weakly increased or even unaffected by stimulation with individual amino acids, whereas supplementation with the “DFGIPV” amino acid mix resulted in strong mTORC1 activation. These results demonstrate the synergistic action of the elevated amino acid levels for mTORC1 signaling pathway activation in chondrogenic cells. Collectively, these findings suggest that the elevated amino acid levels stimulate the activation of mTORC1 in vivo in femur head cartilage.

The mTORC1-dependent downstream biosynthesis machinery is stimulated

mTORC1 is known to coordinate biosynthetic processes, e.g., protein, nucleotide, and lipid biosynthesis, required for basal cellular functions (17), and we therefore studied the enrichment of biosynthesis pathways in the proteome dataset of femur head cartilage. Enrichment analysis showed an overrepresentation of mRNA translation and nucleotide metabolism (ribosome, aminoacyl-tRNA biosynthesis) terms in vivo in CreTW mice compared to control (see Fig. 4B). On the basis of these findings, we used the nonradioactive surface sensing of translation (SUNSET) assay and slot blot analysis on puromycin-treated chondrocytes to study de novo protein biosynthesis (18). A stronger intensity for puromycin pulse-labeled proteins, as a direct measure of protein translation rate, was observed in CreTW chondrocytes compared to control (Fig. 6A). This is in

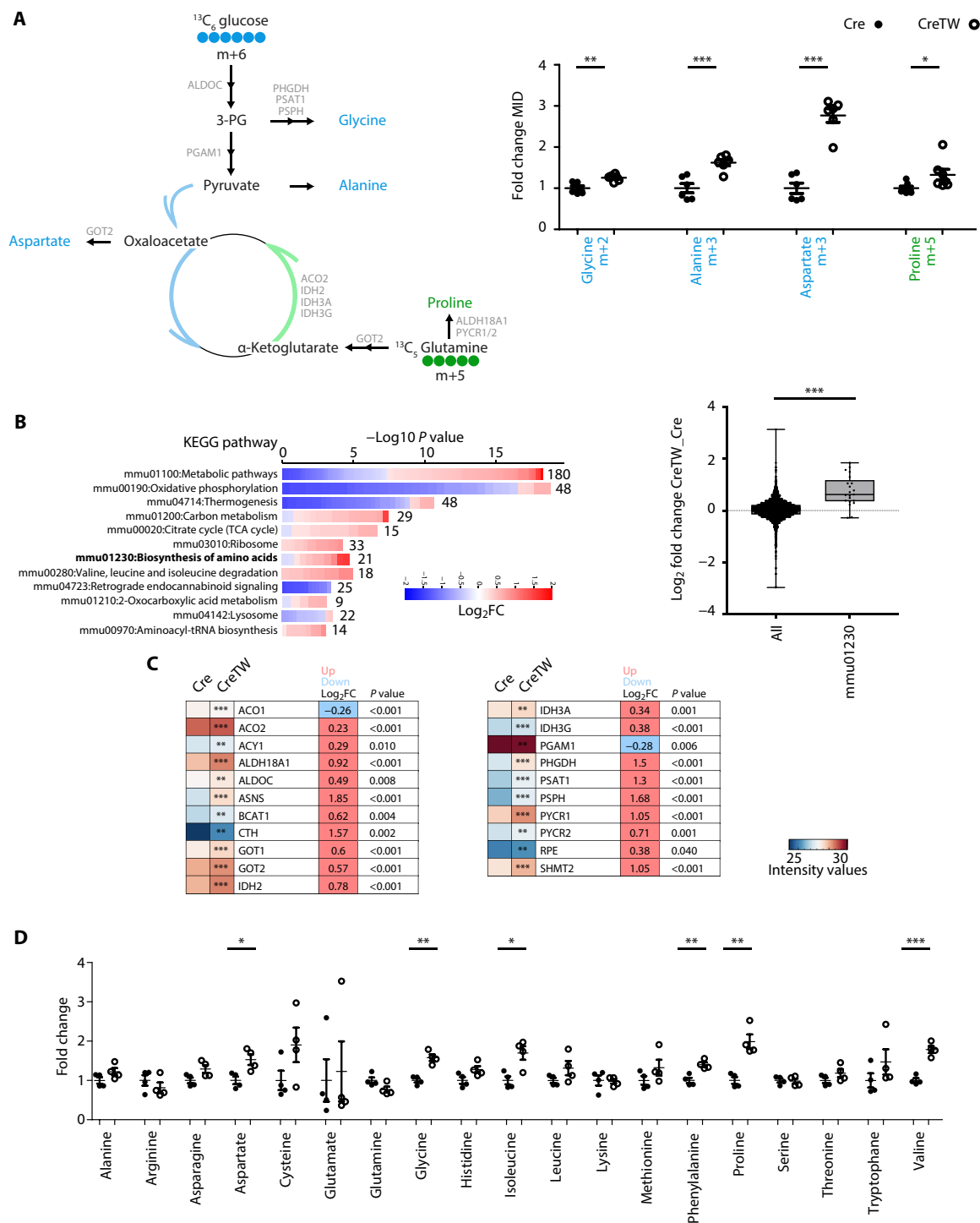


Fig. 4. Rewiring of the TCA cycle can stimulate de novo amino acid biosynthesis in vivo in femur head cartilage with mtRC dysfunction. (A) ¹³C₆ glucose- (glycine, alanine, and aspartate) and ¹³C₅ glutamine-dependent (proline) metabolite enrichment analysis into amino acid biosynthesis pathways using LC-MS-based analysis. Key enzymes are highlighted (scheme, left). Fold changes of the MID between genotypes is given (right, *n* = 6 animals per genotype for ¹³C₆ glucose tracing; *n* = 7 animals per genotype for ¹³C₅ glutamine tracing experiments). Raw data are provided in figs. S4 and S5. (B) KEGG pathway enrichment analysis of differentially abundant entities in femur head tissue extracts from 1-month-old Cre and CreTW mice as determined by mass spectrometry analysis; proteome dataset PXD027109 (8). Terms are ranked according to the mean log₂FC (FC, fold change) and -log₁₀ *P* value. The number of color-coded regulated entities within each pathway is shown, with the corresponding log₂ fold changes of the KEGG mmu01230 pathway Biosynthesis of amino acids summarized in box plot to the right. (C) Mean log₂ fold change (log₂FC, FDR 0.05) of the replicates and significance values are given for the entities of the KEGG category Biosynthesis of amino acids. The direction of fold changes is color-coded: Red indicates entities with increased abundance, while blue represents entities with decreased abundance [(PXD027109 and (8)]. (D) Characterization of the amino acid content in femur head tissue extracts from 1-month-old Cre and CreTW mice using LC-MS-based analysis. Fold changes between Cre and CreTW mice are shown (*n* = 4 animals per genotype). Raw data are provided in fig. S1. Quantitative data are means ± SEM. Unpaired two-tailed Student's *t* test, **P* < 0.05, ***P* < 0.01, ****P* < 0.001.

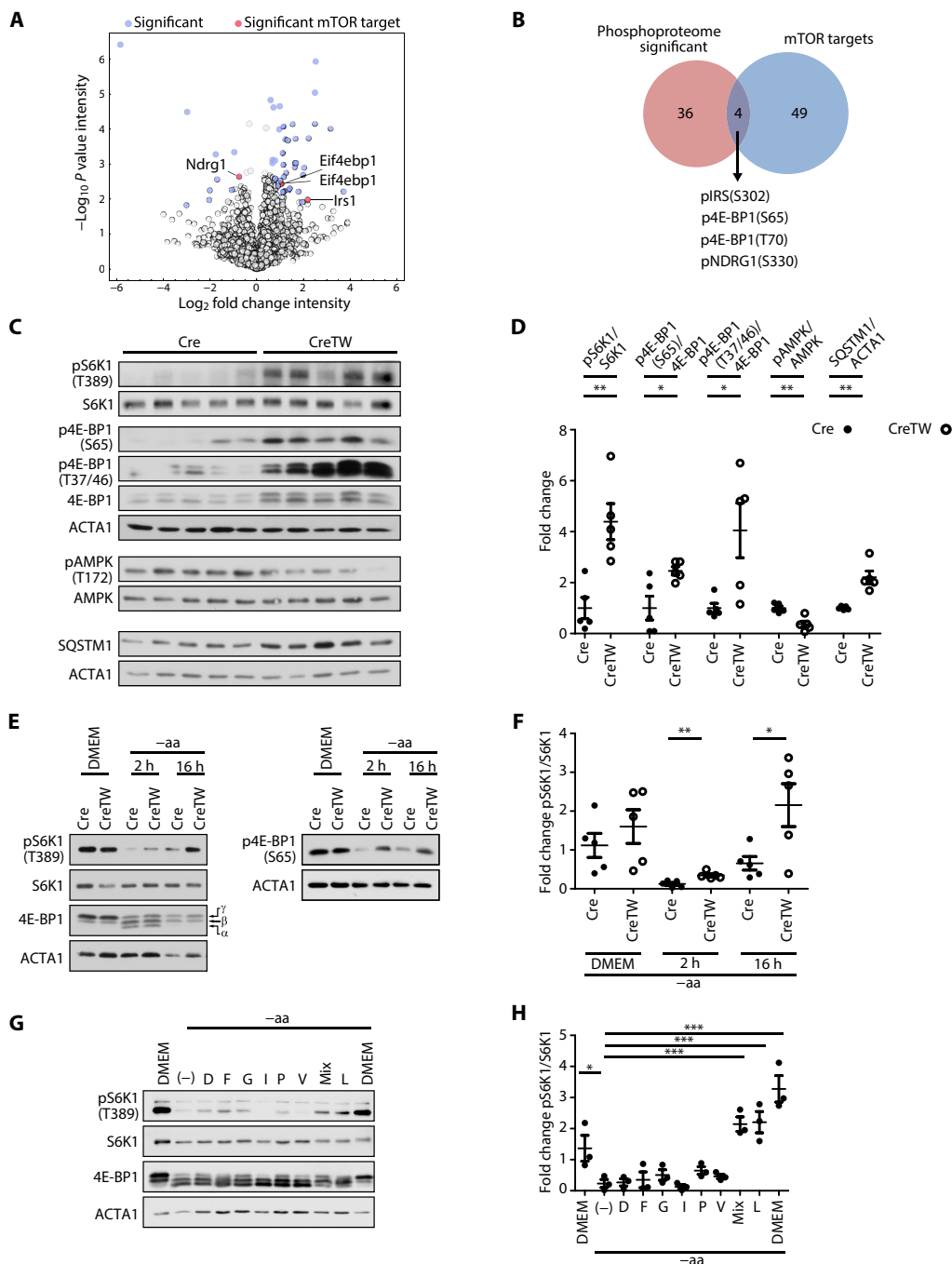


Fig. 5. Metabolic perturbations are sensed by the mTORC1 signaling pathway in femur head cartilage of CreTW chondrocytes. The phosphoproteome of isolated femur head cartilage from 1-month-old Cre and CreTW mice was compared using mass spectrometry. **(A)** The corresponding volcano plot is shown. Differentially phosphorylated entities (blue) and entities associated with the mTOR signaling pathway (red) are highlighted (four biological replicates per group, three animals per group). **(B)** A Venn diagram of enriched mTOR targets with individual phosphorylation sites is shown. **(C)** Immunoblot analysis of regulators and targets of mTORC1 in femur head cartilage extracts from 1-month-old Cre and CreTW mice. ACTA1 was used as a loading control. **(D)** Fold changes between Cre and CreTW mice are shown ($n = 5$ animals per genotype). **(E)** Isolated ribcage chondrocytes from 1-month-old Cre and CreTW mice were cultured in standard growth medium (DMEM) or in amino acid depletion (–aa) medium for 2 and 16 h. Phosphorylation of mTORC1 substrates (S6K1, (p)4E-BP1) was characterized by immunoblot analysis. Hypophosphorylated (α) and hyperphosphorylated forms (β - & γ) of 4E-BP1 are indicated (15). **(F)** Fold changes in S6K1 phosphorylation between Cre and CreTW chondrocytes are shown ($n = 5$ biological samples per genotype). **(G)** Immunoblot analysis of mTORC1 pathway activation in chondrogenic cells cultured in standard growth medium (DMEM, DMEM/F12 10%, FCS 1% PS) or in –aa medium for 2 hours before 2 hours of stimulation with aspartate (D), phenylalanine (F), glycine (G), isoleucine (I), proline (P), valine (V), or the amino acid mixture (DFGIPV mix). Leucine (L) and standard growth medium (DMEM) were used as stimulation control. **(H)** Fold changes in S6K1 protein phosphorylation are shown ($n = 3$ biological samples per genotype). Quantitative data are means \pm SEM, Unpaired two-tailed Student’s *t* test [(D) and (F)] or one-way analysis of variance (ANOVA) with Bonferroni’s multiple comparisons test (H), * $P < 0.05$, ** $P < 0.01$, *** $P < 0.001$.

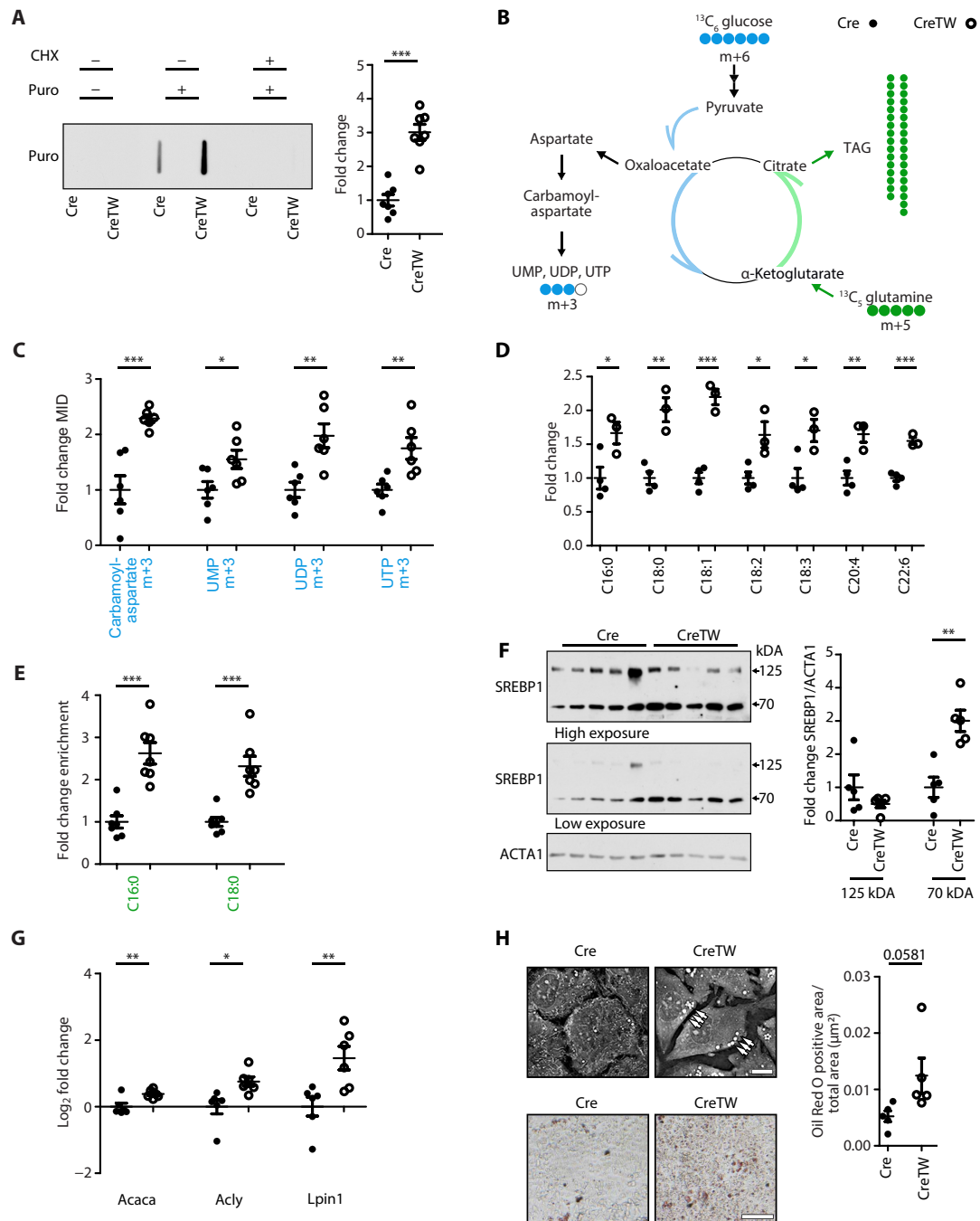


Fig. 6. Biosynthesis processes are stimulated in cartilage with mtRC dysfunction. (A) SunSET assay to sense de novo translation rates in isolated ribcage chondrocytes of 1-month-old Cre and CreTW mice. Slot blot analysis of cells treated with puromycin (Puro). Cycloheximide (CHX) served as control to inhibit translational elongation. Puromycin-incorporation into peptides was determined by immunoblot (left). Fold changes between puromycin-treated Cre and CreTW chondrocytes are shown (graph, $n = 7$ animals per genotype). (B) Scheme of $^{13}\text{C}_6$ glucose carbon enrichment analysis from oxaloacetate into carbamoylaspartate and uridine nucleotide synthesis and $^{13}\text{C}_5$ glutamine carbon enrichment into triacylglycerides (TAG) of cultured Cre and CreTW chondrocytes (scheme). (C) Fold changes of the indicated isotopomers between genotypes are given ($n = 6$ animals per genotype). Raw data are provided in figs. S4 and S5. (D) Mass spectrometry analysis of fatty acyl chain species within the pool of esterified triacylglycerides (TAGs) in femur head cartilage extracts from 1-month-old Cre and CreTW mice. Fold changes are shown ($n \geq 3$ animals per genotype). (E) Fold change enrichment of the palmitic (C16:0) and stearic acids (C18:0) between genotypes is given ($n = 6$ animals per genotype). (F) Immunoblot analysis of SREBP1 levels in cultured chondrocytes. Quantification of full-length (125 kDa) and cleaved (70 kDa) SREBP1 normalized to ACTA1. (G) qPCR analysis of lipogenic genes. Quantitative data are normalized to the mean of *Acta1/Mapk7* and are displayed as log₂ fold change ($n = 6$ animals per genotype). (H) Holotomographic imaging of primary ribcage chondrocytes (top). Lipid droplets are marked with arrows. Scale bar, 10 μm . Oil Red O visualization of neutral lipids. Scale bars, 100 μm . Quantification shows the Oil Red O–positive area normalized to the total area (μm^2), ($n = 5$ biological replicates). Quantitative data are means \pm SEM. Unpaired two-tailed Student's *t* test, * $P < 0.05$, ** $P < 0.01$, *** $P < 0.001$.

line with the increased abundance of many ribosome-related terms when analyzing the proteome signature of CreTW cartilage *in vivo* compared to control. Together, the experiments therefore suggest that mTORC1 activates protein biosynthesis processes in femur head cartilage of CreTW mice. This was further validated by immunofluorescence studies of femur head cartilage *in vivo*, where we observed an increased phosphorylation of the ribosomal protein S6 (S6) as downstream target of the mTOR-S6K1 signaling axis in the central expanded area of femur head cartilage with increased THBS1⁺-containing ECM protein production and deposition (see Fig. 7A).

Presumably, rewiring of the TCA cycle and hyperactive mTORC1 also stimulates nucleotide biosynthesis pathways, and we studied the carbon enrichment into these pathways using ¹³C₆ glucose-labeling experiments (Fig. 6B, blue). Here, an increased enrichment of m+3 intermediates from oxaloacetate to aspartate-carbamoylaspartate into uridine monophosphate (UMP), -diphosphate (UDP), and -triphosphate (UTP) was detected in CreTW chondrocytes compared to control (Fig. 6C). Hence, carbon atoms of the TCA cycle feed preferentially into oxaloacetate/aspartate-dependent pyrimidine synthesis pathways when mtRC is defective. Moreover, the *in vivo* characterization of the proteome in femur head cartilage [PXD027109 (8)] revealed an increase of the multifunctional protein CAD (glutamine-dependent carbamoyl-phosphate synthase: aspartate carbamoyltransferase: dihydroorotase). This enzyme catalyzes three rate-limiting steps of the pyrimidine nucleotide synthesis and is a downstream target of mTORC1 and S6K (19).

Last, we determined the impact of mtRC dysfunction and mTORC1 activation on lipid homeostasis. Characterization of lipid species abundance by mass spectrometry revealed an increase in many nonessential and essential fatty acid subspecies within the pool of triacylglycerides *in vivo* in femur head cartilage of CreTW mice compared to control (Fig. 6D). Accumulation of nonessential fatty acids can result from the reverse influx of glutamine to citrate into acetyl-coenzyme A (CoA)-dependent lipid generation in CreTW chondrocytes (20) as indicated by ¹³C₅ glutamine tracing experiments, where we can detect an increase of glutamine-derived carbons via the TCA cycle into palmitate and stearate in CreTW mice (Fig. 6E). The increase of several essential fatty acids also suggests a contribution from increased uptake or reduced lipolysis/release to the elevated pool of fatty acid subspecies.

Furthermore, active mTORC1 is known to induce the expression of lipogenic genes through SREBP1 cleavage and its translocalization to the nucleus. Here, we detect reduced levels of full-length SREBP1 and increased levels of its shorter, cleaved form, indicative of increased SREBP1 cleavage (Fig. 6F) and an increased expression of genes encoding for key enzymes involved in the lipid pathway (*Acaca*, *Acly*, and *Lpin1*) in chondrocytes of CreTW mice compared to control (Fig. 6G). Moreover, *in vivo* characterization of protein abundance by LC-MS-based analysis [PXD027109 (8)] showed that enzymes, which converts citrate to acetyl-CoA (ACACA) and catalyzes the first-rate limiting step of *de novo* fatty acid biosynthesis from acetyl-CoA to malonyl-CoA (ACLY), are significantly increased *in vivo* in femur head cartilage. Apparently, the activation of the reductive carboxylation pathway and mTORC1-dependent lipogenic enzymes should result in the accumulation of lipids in cells, and we then studied lipid droplet organization *in vivo* in femur head cartilage. Here, we could show by electron microscopy analysis of femur head cartilage an increased number of intracellular lipid droplets in chondrocytes of CreTW cartilage (see Fig. 7C) and confirmed by holotomographic three-dimensional (3D) nanoscopy and Oil red O staining the accumulation of lipid droplets in

isolated chondrocytes (Fig. 6H). Together, the results illustrate that mTORC1 hyperactivation stimulates protein and nucleotide and lead to increases lipid accumulation *in vivo* in cartilage when the mtRC is dysfunctional.

mTORC1 hyperactivation disturbs the autophagy-dependent secretory route

Active mTORC1 promotes cell growth also by inhibiting cellular catabolism through repression of the autophagic flux (21), a process that facilitates the removal of dysfunctional mitochondria and is required to maintain vesicle-mediated transport and ECM secretion during skeletal growth (22). We then studied mTORC1 activation and consequences for autophagy-dependent organelle organization in femur head cartilage. Immunofluorescence studies on paraffin sections of 1-month-old femur head cartilage showed that the ribosomal protein S6 (S6) as downstream target of S6K1 was hyperphosphorylated in the disorganized area of femur head cartilage from CreTW mice but not in control mice (Fig. 7A). This central area of femur head cartilage was previously described to be expanded with increased biomass of THBS1⁺-containing ECM material (8). In addition, immunofluorescence studies detected an increased number of SQSTM1/p62-positive chondrocytes in the disorganized THBS1⁺ area with activated mTORC1 signaling of the femur head cartilage from CreTW mice indicating that autophagy is impaired (Fig. 7B). The increase in total SQSTM1 levels was confirmed by immunoblot and proteome analyses *in vivo* using femur head cartilage from 1-month-old CreTW mice (see Fig. 5C, PXD027109) (8). Moreover, we showed by immunoblot analysis that the turnover of LC3 and SQSTM1/p62 is impaired in isolated chondrocytes from 1-month-old CreTW mice. This shift could be normalized by bafilomycin treatment (fig. S8).

The results show that autophagy is persistently inhibited in cartilage of CreTW mice in regions with accumulation of THBS1⁺ ECM material, increased mTORC1 activity, and defective mtRC. We then applied electron microscopy to understand the consequences of autophagy suppression for intracellular organelle organization in femur head cartilage of CreTW mice. Fragmented mitochondria were mainly found in CreTW chondrocytes but not in the respective control samples. The volume of the endoplasmic reticulum (ER) was frequently expanded, accompanied by a disorganized Golgi apparatus (Fig. 7C). Impaired ER and Golgi apparatus organization can disturb protein folding and secretion processes that are essentially required for ECM formation to stabilize skeletal growth. Proteins of the core matrisome were enriched in the proteome dataset from CreTW cartilage (Fig. 7D). Among those, collagen IX, XI, fibromodulin, matrilin 1, and thrombospondin 1 are well described to modulate collagen fibril assembly and affect ECM secretion and organization. In line with these findings, we previously showed that mtRC failure induces an ECM-specific damage response associated with increased cross-linking and matrix stiffness *in vivo* (8), as well as sensitization of chondrocytes to cell death, premature cartilage degeneration, and growth plate closure (6). Therefore, these results illustrate that hyperactive mTORC1 interferes with the autophagic flux, ER-Golgi-dependent ECM formation processes that eventually contribute to growth plate cartilage degeneration.

Redox imbalances are key targets to restore chondrocyte survival

Our results pointed to an activation of the reductive/reverse TCA cycle that stimulate mTORC1-dependent disturbance of organelle recycling and ECM assembly and secretion processes together with

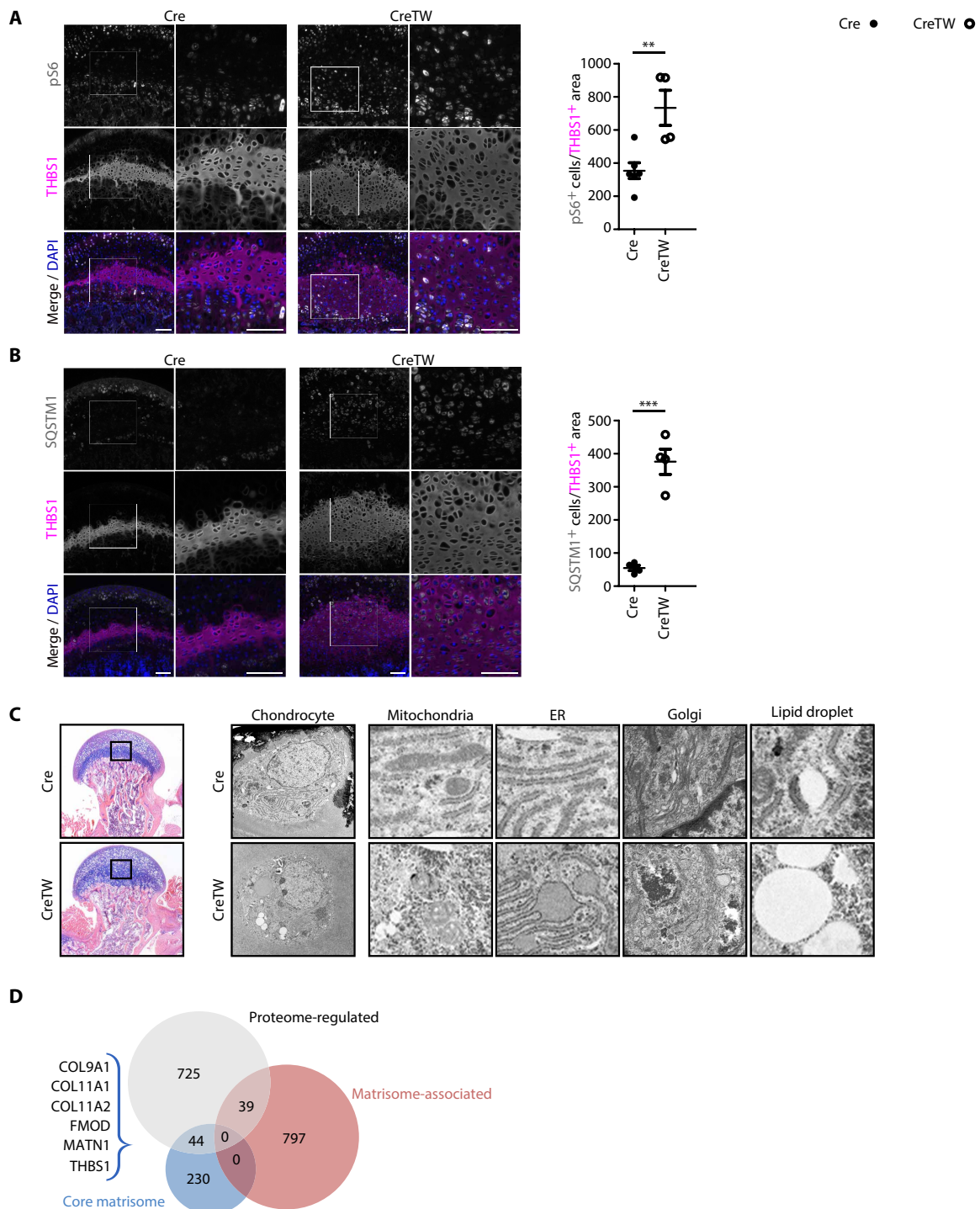


Fig. 7. Autophagy, organelle organization, and core matrisome composition are disturbed in chondrocytes with mtRC dysfunction. (A) p56 (Ser240/244) and THBS1 immunostaining on plane-matched paraffin sections of femur head cartilage from 1-month-old Cre and CreTW mice. Enlarged regions of interest (squares) are shown. The ratio of p56⁺ cells within the THBS1⁺ area was determined ($n \geq 4$ animals per genotype). (B) SQSTM1/p62 and THBS1 immunostaining on plane-matched paraffin sections of femur head cartilage from 1-month-old Cre and CreTW mice. Enlarged regions of interest (squares) are shown. The ratio of SQSTM1/p62⁺ cells within the THBS1⁺ area was determined ($n = 4$ animals per genotype). (C) Alcian blue/hematoxylin and eosin–stained sections of 1-month-old femur heads from Cre or CreTW mice. Electron microscopy analysis of chondrocytes in the THBS1⁺ region from femur head cartilage of 1-month-old Cre and CreTW mice. Mitochondria, ER, Golgi, and lipid organization is shown. (D) Venn diagram of differentially regulated matrisome-associated and core matrisome entities in the proteome (PXD027109) of femur head cartilage from 1-month-old Cre and CreTW mice. Quantitative data are means \pm SEM. Unpaired two-tailed Student's *t* test, ** $P < 0.01$, *** $P < 0.001$. Scale bars, 100 μ m (A) and (B).

the amino acid biosynthesis machinery in CreTW mice. Amino acids can be key signals to recruit mTORC1 to the lysosome surface for activation (23) and may drive mTORC1 activation to sustain fundamental biosynthetic and secretory functions necessary for cell survival when mTORC1 is dysfunctional.

Therefore, we tested how CreTW chondrocytes, which show elevated mTORC1 activity even when cultured in $-AA$ media, respond to long-term amino acid starvation. Here, down-regulation of mTORC1 activity upon amino acid withdrawal is part of an important adaptive cellular response to nutrient insufficiency, as cells with aberrantly hyperactive mTORC1 cannot properly switch off anabolic functions despite the apparent metabolic imbalance leading to cell death (see Discussion). Microscopy analysis revealed a notable decrease in CreTW chondrocyte growth after 3 days in culture when exposed to amino acid-depleted conditions, as opposed to control cells (Fig. 8A). Combined AnxA5/SytoxB staining and flow cytometry analysis (24) showed that the proportion of dying cells was strongly increased in cultures of CreTW chondrocytes upon long-term amino acid depletion compared to Cre control (Fig. 8, B and C). These findings illustrate the detrimental impact of chronic hyperactive mTORC1 signaling under metabolic challenging conditions, a situation also observed in the avascular growth plate cartilage during skeletal growth, where cell death is induced when mTORC1 is defective (6, 8).

We then hypothesized that restoring redox balance could alleviate the effects of amino acid starvation on fundamental biosynthetic functions and cell survival. To test this, we treated amino acid-starved chondrocytes with nicotinamide mononucleotide (NMN), a compound known to boost NAD^+ levels and address redox imbalance in cases of mTORC1 dysfunction (25), and with rapamycin to fully suppress mTORC1 signaling. In this context, the reduction in cell numbers was ameliorated in CreTW chondrocytes supplemented with increasing concentrations of NMN, compared to amino acid-starved and rapamycin-treated cells as shown by microscopy analysis (Fig. 8A). Flow cytometry analysis revealed that the proportion of dying cells was increased in cultures of CreTW chondrocytes upon amino acid depletion and rapamycin treatment (24), while the supplementation with increasing concentrations of NMN strongly reduced cell death (Fig. 8B), presumably by correcting the extreme reducing conditions and stimulating oxidative metabolic pathways. The results reveal that redox imbalances are key targets to restore chondrocyte survival and to prevent cartilage degeneration and premature aging processes caused by mitochondrial dysfunction.

DISCUSSION

Patients with mitochondrial diseases show signs of increased energy-consuming biosynthetic processes associated with lifespan reduction

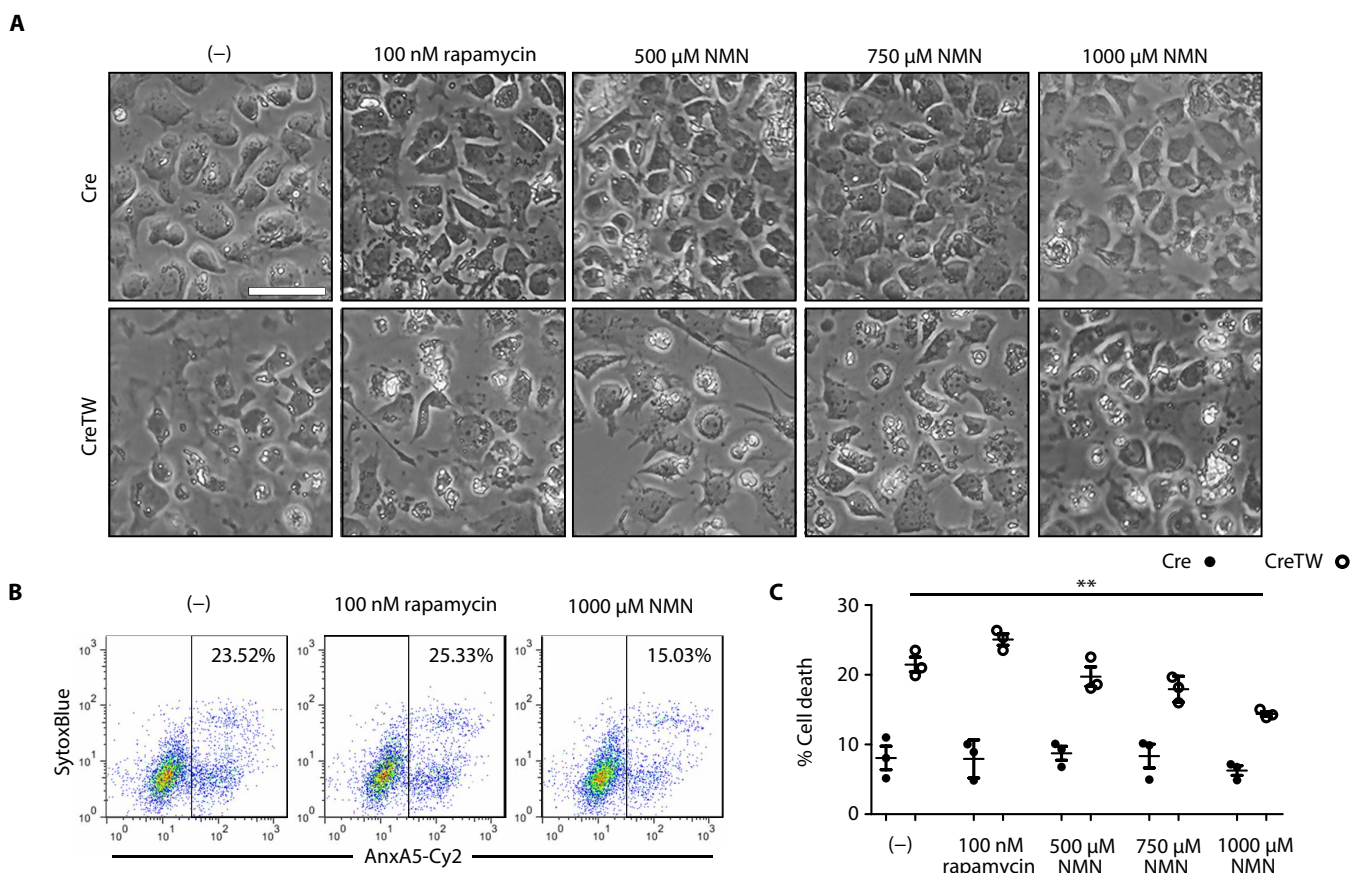


Fig. 8. NMN supplementation ameliorates cell death of chondrocytes with mTORC1 dysfunction. Chondrocytes from 1-month-old Cre and CreTW mice were cultured for 3 days in $-aa$ medium in the absence (-) or presence of rapamycin or increasing concentrations of NMN. (A) Cell morphology was studied by microscopy and (B) cell death by flow cytometry. (C) The proportion of AnxA5-Cy2⁺/SytoxBlue⁻ and AnxA5-Cy2⁺/SytoxBlue⁺ dying cells is given ($n = 3$ litters per group). Quantitative data are means \pm SEM. One-way ANOVA with Bonferroni's multiple comparisons test, $**P < 0.01$. Scale bar, 50 μ m.

and growth retardation. It was previously proposed that this metabolic response protects cells from acute mtRC defects yet with potential long-term consequences for aging processes (4). Here, we provide a molecular scenario for how energy-consuming biosynthetic pathways are redirected in cells to compensate for the loss of mtRC activity but paradoxically trigger premature aging of growth plate cartilage. Moreover, we demonstrate how this knowledge can be used to target metabolic pathways and ameliorated cell death as a central outcome of mtRC dysfunction and skeletal aging phenotypes in mitochondrial disease.

The TCA cycle operates in reverse to sustain the metabolite supply

The metabolite analysis by LC-MS-based analysis showed that lactate levels are elevated as a consequence of increased glycolytic activity in adult cartilage with mtRC dysfunction. This metabolic shift toward glycolysis-driven lactate production was previously observed in cell lines with impaired mtRC, where glycolysis is engaged to produce energy and recycle NADH to NAD⁺ by oxidation of pyruvate into lactate (26), and lactate may also be released from cartilage to cause systemic lactic acidosis as observed in mutants with an epidermis-specific expression of the Twinkle mutant helicase (27). Here, the rewiring of the metabolism in skin epidermis results in high lactate levels in blood contributing to early postnatal death of the mice. However, we did not observe systemic metabolic effects of mitochondrial dysfunction in CreTW mice with a cartilage-specific expression of the Twinkle mutant helicase. CreTW mice have no impairment in survival rate (6) and changes in the blood pH, lactate, or glucose levels (fig. S9), and our detailed analysis of the phosphoproteome did not provide evidence for the activation in the insulin or growth hormone pathways that may act systemically on skeletal growth. Cartilage is avascular, meaning that it lacks blood vessels and, as a result, accumulated lactate and any other metabolites cannot be quickly distributed via the bloodstream as compared to other tissues. Therefore, we conclude that the metabolic phenotype of CreTW mice is restricted to cartilage, where we unexpectedly observed a strong impact of mtRC dysfunction on TCA cycle metabolism. We detected a higher abundance of the TCA cycle metabolites and enzymes indicative of an increase in TCA cycle activity and metabolite production. The findings were rather unexpected as lack of electron transfer to the respiratory chain results in excess of NADH, which inhibits the function of pyruvate dehydrogenase complex and the metabolic flow of the TCA cycle (28–31). Apparently, the TCA cycle has a remarkable flexibility and reversibility in mammalian cells to sustain the metabolite supply in challenging situations when respiration is impaired (32–34).

An anaplerotic replenishment of carbons into the TCA cycle can lead to reductive/reverse orientation of the cycle when OXPHOS is impaired (9). We now provide evidence that two sections of the reverse TCA cycle bypass the shortage in TCA cycle metabolites in chondrocytes with mtRC dysfunction. The use of the isotopic tracer ¹³C₆ glucose shows a carbon enrichment into the first segment of the reverse TCA cycle from pyruvate to oxaloacetate up to succinate. This segment runs counterclockwise only under very strong reductive conditions when the lack of mtRC dysfunction forces the SDH complex to reduce fumarate to succinate (9). The latter cannot be converted back to α -ketoglutarate due to the unidirectional nature of the reaction from α -ketoglutarate to succinyl-CoA (35), and, therefore, LC-MS-based analysis detects a strong accumulation of

succinate in cartilage of CreTW mice. In addition, ¹⁵C₅ glutamine tracing experiments revealed a carbon enrichment into a second segment of the reverse TCA cycle from glutamine to α -ketoglutarate into citrate. Activation of this second segment of the TCA cycle was associated with an increase of involved metabolites (α -ketoglutarate to citrate), enzymes (ACO2, IDH3, and ACLY), and transporters (e.g., SLC25A1) as shown by mass spectrometry. This segment, alternatively referred to as glutamine-dependent reductive carboxylation pathway in the setting of respiratory dysfunction (32), was described to support chondrocyte growth and matrix production under glycolytic conditions (36), and we now demonstrate its importance for chondrocytes experiencing mtRC dysfunction. In conclusion, glutamine and pyruvate act as alternative anaplerotic carbon sources that are redirected into two distinct sections of the reverse TCA cycle to sustain the metabolite generation in chondrocytes with impaired mtRC. This reverse TCA cycle activity and pyruvate/glutamine metabolism are tightly coupled to produce metabolites for biosynthesis reactions. Moreover, metabolites of the reverse TCA cycle function as alternative electron acceptors to regenerate NAD⁺ in response to a reductive shift when electron flow to oxygen is impaired (9). Therefore, the redirecting of the TCA cycle fulfills a dual function: producing TCA cycle intermediates and replenishing NAD⁺ to sustain the biosynthetic pathways in growth plate cartilage with defective mtRC. Proline and aspartate synthesis pathways were previously described to facilitate NAD⁺ regeneration in cells with a disturbed electron transport chain (37, 38), and the engagement of these pathways in CreTW chondrocytes may further support the regeneration of NAD⁺. However, the activation of the reverse TCA cycle and its associated amino acid synthesis pathways could not fully restore redox/energy homeostasis in the long term. The NAD⁺/NADH ratio and ATP levels were still significantly reduced in cartilage of 1-month-old CreTW mice [see Fig. 2E and (6)]. Last, amino acid biosynthesis pathways may also be activated to eliminate the excess of glutamine-derived amino groups and sustain the metabolic input into the reductive carboxylation pathway. Therefore, the redirecting of the TCA cycle efficiently restores metabolites but imposes a higher energetic expense for these biosynthesis processes. This scenario was predicted by stochastic modeling of patients with mitochondrial diseases (39), and we now provide a molecular explanation for the increased metabolic expenses of mitochondrial diseases.

Rewiring of the TCA cycle can stimulate amino acid biosynthesis and mTORC1 signaling

We show here that de novo amino acid biosynthesis, as a result of metabolic rewiring of the TCA cycle, contribute to the activation of mTORC1 signaling in chondrocytes when mtRC is dysfunctional. Protein degradation and amino acid uptake from extracellular sources may further assist to the increase in amino acid levels. However, at present, our glutamine uptake experiments suggest that uptake plays a relatively minor role in this context (fig. S6). TCA cycle metabolites can feed directly into amino acid biosynthesis pathways to increase a distinctive profile of amino acid in cartilage as demonstrated by the carbon tracing, proteome, and amino acid profiling experiments. We detect a synergistic stimulatory impact of the elevated amino acids on mTORC1 activity in chondrogenic cells as we observe a robust activation of the mTORC1 signaling pathway driven by supplementation with the mix of all amino acids whose levels are elevated in CreTW chondrocytes but not by individual amino acids. These results suggest that endogenous amino acids may serve

as primary signals to sustain basal levels of mTORC1 activity in chondrocytes with defective mtRC, even under conditions of exogenous amino acid withdrawal. Notably, upon longer starvation times, this aberrant mTORC1 activation causes chondrocyte cell death (6), presumably due to a metabolic imbalance of nutritional demand and supply, as well as due to suppression of autophagy. Inhibition of autophagy can compromise the degradation of substrates regulated by the ubiquitin-proteasome pathway (40), potentially feeding back to the mTORC1 signaling pathway. Notably, the mTOR target 4E-BP1 is known to undergo ubiquitination and subsequent degradation by the proteasome (41), and it is tempting to speculate that the observed increase in 4E-BP1 levels (see Fig. 5C) may result from impaired proteasomal degradation under conditions of dysfunctional mitochondrial respiration. A rapid autophagic response is typically necessary to protect cells from cell death, and similar examples were reported in previous studies using different models of aberrant mTORC1 activation or dysregulated translation that can lead to cellular or organismal death when combined with nutrient deprivation (23, 42–46). Endogenous TCA cycle-derived amino acids cannot fully restore mTORC1 activity, and cells undergo cell death after metabolic stress. Here, we could improve CreTW chondrocyte survival by providing the external NMN to regenerate NAD^+ levels and stimulate oxidative metabolic pathways, whereas cell death was increased after supplementation with rapamycin and total inhibition of mTORC1 activity. Therefore, basal mTORC1 activation is essential for maintaining cell survival when mitochondrial respiration is impaired, but both its hyperactivation and complete inactivation are detrimental to cell survival. Redox imbalances are key targets for restoring chondrocyte survival to maintain an oxidative microenvironment and are crucial for biochemical pathway activation and for preventing cartilage degeneration and premature aging caused by mitochondrial dysfunction. Previous studies have shown that nicotinamide precursor supplementation can ameliorate phenotypes linked to mitochondrial dysfunction in vivo (25, 47), and our work now provides a mechanistic explanation for why these experiments are effective and reveals a therapeutic potential for rescuing skeletal aging response when mtRC is dysfunctional. The findings highlight the sensitivity of chondrocytes to redox balances as well as the importance of these pathways for chondrocyte survival when mtRC is defective. It may also explain why cell death is increased in late hypertrophic chondrocytes when mtRC is dysfunctional (6, 8). Late hypertrophic chondrocytes activate OXPHOS to face additional bioenergetic challenges with the increased oxygen availability supplied by invading blood vessels at the chondroosseous junction (6, 48). Here, the failure to activate mtRC in CreTW mice may impose further metabolic stress and trigger cell death.

The metabolic-signaling response accelerates cartilage degradation

It is the primary function of the mTORC1 signaling pathway to stimulate biosynthetic activities, and in this context, we detect the highest mTORC1 signaling activity in regions with excessive production of ECM material and lipid droplet accumulation in femur head cartilage in vivo. Therefore, hyperactive mTORC1 drives biosynthetic processes required for skeletal growth when mtRC is dysfunctional but also may cause a local overproduction of proteins and lipids. The latter is frequently observed in other mouse mutants with mitochondrial dysfunction. Here, mice with specific ablation of the mitochondrial aspartyl-tRNA synthetase DARS2, the respiratory

chain subunit SDHA or the assembly factor COX10 in intestinal epithelial cells showed accumulation of large lipid droplets (49), which was attributed to impaired trafficking of chylomicrons from the ER to the Golgi. We now expand this understanding of the impact of mtRC dysfunction on lipid metabolism and show that mtRC dysfunction in cartilage activates mTORC1-dependent expression of lipogenic key enzymes and the glutamine-dependent reductive carboxylation pathway to stimulate nonessential lipid biosynthesis processes in vivo. Moreover, the increased abundance of essential fatty acids in cartilage suggests a contribution from enhanced lipid uptake and/or reduced lipolysis or release, both of which may be regulated by the mTORC signaling pathway (50). These results add a biochemical explanation for the accumulation of lipids observed in many mouse mutants with mitochondrial dysfunction in vivo.

The mTORC1 signaling pathway is a critical inhibitor of autophagy to hinder organelle removal, and the latter could be crucial to equilibrate cellular responses in chondrocytes with defective mitochondria. It was earlier proposed that cells shut down autophagy to prevent the total loss of dysfunctional mitochondria in the long term and sustain their basal biosynthetic activity (51). This concept is in line with the observation that degradation of organelles is impaired after chronic mtRC inhibition by long-term treatment with rotenone (52). Moreover, yeast lacking the mt genome and RC activity show a reduction in the autophagic flux (53), and human embryonic kidney 293 cells with chronic genetic defects in complex I activate the mTORC1 signaling pathway to suppress autophagy (54). In agreement with these results, we detected an impairment of the autophagic flux in cartilage with fragmented mitochondria, disturbed ER-Golgi organization, and altered ECM secretion and extracellular assembly (6, 8). Hence, mTORC1 signaling pathway could be activated to prevent total removal of defective yet biosynthetically active mitochondria in chondrocytes via autophagy, whereas its prolonged suppression disturbs organelle to impair ECM secretion process and destabilizes growth plate cartilage.

The importance of the mTORC1 signaling axis for skeletal aging is also illustrated by the phenotype of mice with chronic activation of mTORC1 in cartilage. Col2a1-Cre-driven deletions of TSC1 to activate mTORC1 signaling in cartilage results in short stature and chondrodysplasia associated with reduced amounts of collagen X and MMP13 (55). Growth retardation/chondrodysplasia as well as impaired collagen X and MMP13 deposition are not only features of our CreTW mutants with mtRC dysfunction in cartilage (6) but also of those with defective autophagy in chondrocytes (22). Cartilage-specific deficiency of *Atg7*, the protein product that is required for autophagosome membrane formation and inhibition of autophagic activity, triggers ER stress associated with dilated ER cisternae, reduced secretion of collagens II and IX due to retainment in the defective ER, and ultimately, increased cell death.

These notable molecular and phenotypical similarities between mutants support our view that chronic reductive TCA cycle activity is sensed by amino acid-dependent stimulation of mTORC1 signaling and inhibits the elimination of defective mitochondria by autophagy. There are costs associated with this response, which is the increased disruption of the secretory pathway and the ECM as a whole, as well as premature growth plate degeneration and aging.

Overall, our findings underscore the importance of the reverse TCA cycle and the amino acid-dependent activation of the mTORC1 signaling pathway to equilibrate cellular responses in cartilage (Fig. 9). This adaptation increases the metabolic expenses for skeletal growth

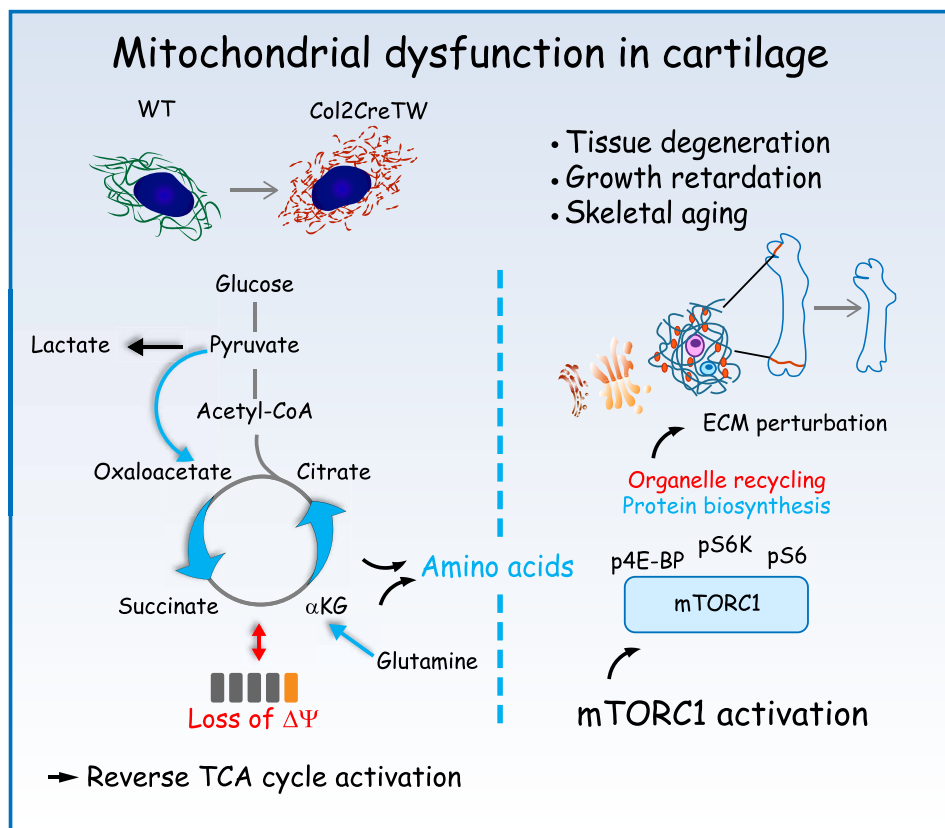


Fig. 9. Molecular consequences of mitochondria dysfunction in cartilage for skeletal aging processes. The reverse TCA cycle is activated to replenish carbon loss due to dysfunctional electron transport chain (ETC) in CreTW cartilage and increases amino acid levels to activate the mTORC1 signaling pathway. mTORC1 hyperactivation disturbs organelle and ECM organization associated with age-related chondrocyte death and premature cartilage degeneration.

over time and reduces the lifespan of growth plate cartilage leading to growth impairment as a sign of premature skeletal aging, a phenomenon frequently observed in patients with mitochondrial disease. Restoring the redox balance by boosting NAD^+ to activate oxidative metabolism can be a key target to ameliorate these consequences and improve the aging outcome.

MATERIALS AND METHODS

Mouse breeding and tissue collection

All experiments were performed in accordance with the German animal protection law (Institutional Review Board: "Landesamt für Natur, Umwelt und Verbraucherschutz Nordrhein-Westfalen"). Transgenic Col2a1-Cre C57BL/6 mice with cartilage-specific mtRC dysfunction (CreTW) (6) were generated by breeding mice expressing Cre recombinase under the control of a Col2a1 promoter (Col2a1-Cre C57BL/6N) (56) with R26-K320E-Twinkle^{loxP/+} animals (Fig. 1A) (27). Standard irradiated mouse chow and water was supplied ad libitum. Femur head tissue extracts were collected from female 1-month-old mice (± 1 day) after cervical dislocation and snap frozen in liquid nitrogen. Heterozygous Col2a1-Cre-R26-K320E-Twinkle^{loxP/+} mice (CreTW) were compared to Col2a1-Cre (Cre) littermates.

Isolation of primary ribcage chondrocytes and cell culture

The ribcage of female 1-month-old mice was used to isolate sufficient numbers of primary chondrocytes. Femur head tissue could

not be used because of insufficient yield in cell numbers. Dissected ribcages were preincubated in collagenase P [2 mg/ml in Dulbecco's modified Eagle's medium (DMEM)/F12, 10% fetal calf serum (FCS), and 1% (100 U/ml) penicillin-streptomycin (P/S)] for 30 min, and the adherent connective tissue was removed and chondrocytes isolated by collagenase II digest (450 U/ml in DMEM/F12, 10% FCS, and 1% P/S) over night (18 to 20 hours). Isolated rib cage chondrocytes were cultured in DMEM/F12, 10% FCS, 1% P/S, ASC [ascorbate (44 μ g/ml; Sigma-Aldrich), and L-ascorbate-2-phosphate (130 μ g/ml; Sigma-Aldrich)] at 37°C/5% CO_2 . After 24 hours, chondrocytes were detached by collagenase II (2 mg/ml in DMEM/F12, 10% FCS, and 1% P/S) incubation for 1 hour, centrifuged, resuspended in medium, and plated in 45,000 cells per 48-well unless otherwise stated. ATDC5 cells, a chondrogenic cell line, was grown at 37°C/5% CO_2 in DMEM/F12, 5% FCS, and 1% P/S and used for stimulation experiment 24 hours after plating.

Paraffin sections and immunofluorescence analysis

Femora of 1-month-old mice were isolated and fixed in 4% paraformaldehyde overnight. After 4 weeks of decalcification in 0.5 M EDTA (pH 8), by changing the solution once a week, femora were embedded in paraffin and sectioned (7 μ m) using a microtome (HM355 S, Thermo Fisher Scientific, Waltham). The organization of the femur head cartilage was assessed by hematoxylin/eosin/Alcian blue staining. Moreover, target proteins in femur cartilage were analyzed by immunofluorescence. To unmask epitopes, the sections

were incubated with hyaluronidase (5 mg/ml; Sigma-Aldrich) for 30 min at 37°C and proteinase K (10 µg/ml; Sigma-Aldrich) for 10 min at 50°C. The following primary antibodies were used: mouse anti-THBS1 (1:1000, Santa Cruz Biotechnology), rabbit anti-pS6 (1:100, CST, #5364), and rabbit anti-SQSTM1 (1:200, MBL, #PM045). Corresponding secondary antibodies coupled to Cy3 (1:800, Jackson ImmunoResearch) or Alexa Fluor 488 (1:1000, Invitrogen, Thermo Fisher Scientific) were used to visualize the binding of the primary antibody. Sections were analyzed using a Nikon Eclipse TE2000-U microscope (Nikon). Brightness and contrast were adjusted for visualization.

SDS-PAGE and immunoblotting

Femur head cartilage of 1-month-old mice was lysed in 80 µl of radioimmunoprecipitation assay (RIPA) buffer containing 5% NP-40, 0.25% Triton X-100, 2.5% 750 mM NaCl, and 100 mM tris-HCl (pH 7.4) supplemented with protease inhibitor (#P8340, Sigma-Aldrich) and phosphatase inhibitor (#4906837001, Sigma-Aldrich) cocktails and incubated overnight at 4°C. Cultured primary chondrocytes as well as stimulated ATDC5 cells in 48-well plate were lysed in 60 µl of RIPA buffer supplemented with inhibitor cocktails, disrupted by sonication (20 s, 60% amplitude, Branson), and debris was removed by centrifugation before SDS-polyacrylamide gel electrophoresis (SDS-PAGE). Equal amounts of protein lysates were loaded, and proteins were transferred to a nitrocellulose membrane (Whatman) or polyvinylidene difluoride membrane (IPVH00010, Merck Millipore) for SREBP1 protein detection. Membranes were stained with Ponceau S (Serva) and blocked with 5% nonfat dry milk or bovine serum albumin in TBS-T buffer [50 mM tris-HCl (pH 7.4), 150 mM NaCl, and 0.1% Tween-20], before adding primary antibody overnight at 4°C. The following primary antibodies were used: rabbit anti-4E-BP1 (1:2000, CST), rabbit anti-p-4E-BP1 S65 (1:500, CST), rabbit anti-p-4E-BP1 T37/46 (1:1000, CST), rabbit anti-p-AMPK T172 (1:1000, CST), rabbit anti-AMPK (1:1000, CST), rabbit anti-p-S6K1 T389 (1:1000, CST), rabbit anti-S6K1 (1:1000, CST), anti-rabbit SQSTM1 (1:1000, MBL), mouse anti-SREBP1 (1:500, Thermo Fisher Scientific), and ACTA1 (1:2000, Millipore). After washing with TBS-T buffer the corresponding secondary antibody labeled with horseradish peroxidase (DAKO, Santa Clara) was added for 1 hour at room temperature (RT). Antibody binding was visualized by enhanced chemiluminescence (ECL) using 10 mM tris (pH 8.8), 12.5 µM luminol, 2.3 µM coumaric acid, and 5.3 µM hydrogen peroxide, or Amersham ECL Prime Western Blotting detection reagent (VWR) or Trident femto Western HRP Substrate (Gentex) depending on the primary antibody. To detect chemiluminescence signal x-ray films (Valmex) were used. Exposure was adjusted to the linear range, and band intensities were quantified via ImageJ software.

Cellular treatments

Primary isolated ribcage chondrocytes were precultured for 24 hours before amino acid starvation. Standard growth medium (DMEM/F12, 10% FCS, 1% P/S, and ASC) was removed, and cells were carefully washed for two times with phosphate-buffered saline (PBS). Amino acid-free DMEM/F12 (D9811-01, US Biologicals) containing 10% dialyzed FBS (F0392, Sigma-Aldrich) and 1% P/S was applied for 2 and 16 hours of incubation. Rapamycin (100 nM; LC-Laboratories R-5000) or 500, 750, and 1000 µM of NMN (Sellack chemicals GmbH S5259) were supplemented for cell death rescue experiments.

ATDC5 cells were similarly plated and starved for amino acids. Single amino acids [aspartate (D), phenylalanine (F), glycine (G), isoleucine (I), proline (P), valine (V)], amino acid mixture containing all six amino acids (D + F + G + I + P + V), leucine (L), and standard growth medium (DMEM/F12, 10% FCS, and 1% PS) as a stimulatory control were supplied to amino acid-free DMEM/F12 [DMEM/F12 amino acid-free, 10% dialyzed FCS (Sigma-Aldrich), and 1% P/S] in a five times higher concentration than in DMEM to mimic the described accumulation in CreTW cartilage. Cells were lysed accordingly and subjected for further SDS-PAGE/immunoblot analysis.

NAD/NADH quantitation

Femoral heads were isolated from 1-month-old animals, immediately snap-frozen in liquid nitrogen, and stored at -80°C until further processing. The NAD/NADH ratios were determined using a NAD/NADH quantification kit (Sigma-Aldrich) following the manufacturer's instructions.

Surface sensing of translation

Primary isolated chondrocytes were seeded at a density of 15,000 cells per 48-well plate. Cells were either untreated or pretreated with the translation inhibitor cycloheximide at a concentration of 10 µg/ml for 5 min before labeling with puromycin. Subsequently, puromycin (10 µg/ml) was added for 10 min to enable its incorporation into nascent peptides. The cells were then lysed using RIPA buffer, and 20 µl of the resulting lysate was applied to a nitrocellulose membrane using vacuum (slot blot analysis). A puromycin antibody at a dilution of 1:7500 in 5% milk TBS-T (MABE343, Sigma-Aldrich) followed by the corresponding secondary antibody labeled with horseradish peroxidase (DAKO, Santa Clara), and chemiluminescence was used to detect the puromycin incorporation.

Triacylglycerol detection

Samples of snap-frozen femur head tissue of 1-month-old mouse were pulverized using 2.8-mm ceramic beads (CK28 hard tissue homogenizing tubes, Precellys tissue homogenizer, Bertin) at 0°C for 3 × 20 s at 6800 rpm with 30-s breaks. Pulverized tissue was homogenized in Milli-Q water (1 mg/10 µl). The protein content of the homogenate was routinely determined using bicinchoninic acid.

To 50 µl of the homogenate 450 µl of Milli-Q water, 1.875 ml of methanol/chloroform 2:1 (v/v) and internal standards (40 µl of d5-TG Internal Standard Mixture I, Avanti Polar Lipids) were added. Lipid extraction was performed as previously described (57).

Triacylglycerols were analyzed by nano-electrospray ionization (ESI) tandem mass spectrometry with direct infusion of the lipid extract (Shotgun Lipidomics) as previously described (57–59). Endogenous lipid species were quantified by referring their peak areas to those of the respective internal standard. The calculated lipid amounts were normalized to the protein content of the tissue homogenate.

Lipid visualization in cell culture using label-free holotomographic imaging and Oil Red O staining

Primary isolated ribcage chondrocytes were plate in Ibidi dishes (µ-dish 35 mm, low, ibi-treated, Thermo Fisher Scientific), cultured for 3 days, and analyzed by label-free holotomographic imaging (3D Cell Explorer-fluo, Nanolive). The measurement of the refractive index enables visualization of the mitochondrial network and lipid

droplets without using additional staining. Brightness and contrast were adjusted for better visualization, equally.

Oil Red O staining was conducted on primary isolated chondrocytes after 7 days of culture. First, the cells were fixed for 5 min using ice-cold MeOH, were washed with tap water, and incubated with 60% isopropanol for 5 min. Six parts of the Oil Red O stock solution (0.5 g of Oil Red O per 100 ml 99% isopropanol) were freshly diluted with four parts Aqua Dest and immediately used to incubate the cells for 20 min. Last, the cells were differentiated for 5 min with 60% isopropanol and washed with Aqua Dest. Pictures of stained cell layer were taken using Nikon Eclipse TE2000-U microscope. Quantification of Oil Red O stained area was conducted using ImageJ software and data was analyzed and visualized using GraphPad Prism.

RNA isolation, quality control, and quantification by qPCR

Adherent chondrocyte cultures were cultured for 7 days and collected in TRIzol Reagent (Life Technologies), and RNA was isolated by phenol-chloroform extraction. The concentration was determined using the NanoDrop 2000 spectrophotometer (Thermo Fisher Scientific, Darmstadt, Germany), and RNA quality was assessed by micro-capillary electrophoresis (2100 Bioanalyzer, Agilent, Santa Clara, CA) according to the manufacturer's specifications. One microgram of nondegraded RNA with an RNA integrity number above 8 was reversely transcribed using Omniscript Reverse Transcription Kit (Qiagen) according to manufacturer's recommendations. cDNA (5 ng/5 μ l) was used for the Takyon No ROX SYBR 2X MasterMix dTTP Blue (Eurogentec) in a total volume of 20 μ l in clear FrameStar 96 semi-skirted plates (4titude, Dorking, UK). Thermal cycling parameters were 3 min at 95°C followed by 40 cycles of 10 s at 95°C, 20 s at 60°C, and 40 s at 72°C. Gene-specific primers (Sigma-Aldrich, Darmstadt, Germany) were used for the detection of *Acaca*, *Acly*, *Actb*, and *Lpin1 Mapk7*. Quantitative polymerase chain reaction (qPCR) analysis was performed with the StepOnePlus Real-Time PCR System (Applied Biosystems, Foster City, CA), and specificity of gene amplification was confirmed by melting curve analysis. Primers used for gene expression analysis are listed (table S1). Multiple reference gene normalization (mean of *Mapk7* and *Actb*) was used to avoid biased misinterpretation of expression data. The fold change (FC) was calculated using the $\Delta\Delta C_t$ method (60), \log_2 -transformed, and displayed on a \log_2 -scaled axis to represent the expression changes in a similar manner across the order of magnitude. Six biological replicates were analyzed per genotype.

Phosphopeptide enrichment and proteomic analysis

Isolated femur head cartilage pooled from three animals was pulverized using 2.8-mm ceramic beads (CK28 Hard tissue homogenizing tubes, Precellys tissue homogenizer, Bertin) at 0°C for 3 \times 20 s at 6800 rpm with 30-s breaks. The resulting powder was mixed with sodium deoxycholate (SDC) lysis buffer [4% (w/v) SDC in 100 mM tris-HCl (pH 8.5)] and immediately heated at 95°C for 5 min before being sonicated. The samples were further processed and measured using the established EasyPhos method (12). Raw files were processed using MaxQuant (version 1.5.3.8) and its implemented Andromeda search engine and LFQ algorithm. Perseus (version 1.5.5.3; Max Planck Institute of Biochemistry) was used to perform the two-sided Student's *t* test and calculate permutation-based false discovery rate ($S_0 = 0.1$; number of randomizations = 500). Data visualization was conducted using Instant Clue software 0.5.2 (University of Cologne) for

volcano plot and intensity value plot generation. Plots were generated using DAVID and the associated Flaski apps (<https://flaski.age.mpg.de>, developed and provided by the MPI-AGE Bioinformatics core facility) using the 12 to 15 most significant KEGG terms from each analysis, after depletion of disease-related terms.

Metabolite extraction of polar metabolite

Metabolites were extracted from snap-frozen femur head tissue of 1-month-old or from primary isolated rib cage chondrocytes after $^{13}\text{C}_6$ glucose and $^{13}\text{C}_5$ glutamine treatment. For the extraction of femur head tissue, the deep-frozen material was pulverized two times for 1 min at 25 Hz in 2-ml Eppendorf tubes (www.eppendorf.com) using a ball mill-type grinder equipped with a 48-sample holder (Tissue Lyser 2; www.qiagen.com). For each sample, one liquid nitrogen-cooled 5-mm stainless steel metal ball was added to the Eppendorf tube. Between the first and the second homogenization, the sample holder with the samples was recooled in liquid nitrogen for 30 s to make sure that the tissue was continuously frozen. Metabolites from these pulverized samples was extracted in 850 μ l of extraction buffer (80% ultra-performance liquid chromatography (UPLC)-grade methanol/water, VWR), which was precooled to -20°C . After the buffer was added, each sample was immediately vortexed until the cell pellet was homogeneously suspended. The samples were then incubated on an orbital mixer at 4°C for 30 min at 1500 rpm (VWR). In a subsequent step, the samples were sonicated for 10 min in an ice-cooled bath-type sonicator (VWR). After sonication, the samples were centrifuged for 5 min at 21100g at 4°C and the cleared, metabolite-containing, supernatant was transferred to fresh 1.5-ml Eppendorf tubes, while the protein-containing pellets were kept for protein quantification (DirectDetect IR spectrometer; Merck Millipore). The collected supernatant was placed into a Speed Vac concentrator (Eppendorf) and concentrated at 30°C to dryness.

Metabolite extraction of primary rib cage chondrocytes was performed after 120 min of 68% heavy glucose [$^{13}\text{C}_6$ glucose (2151 g/liter) and glucose (1 g/l $^{12}\text{C}_6$)] treatment in alpha minimum essential medium and after 1 and 24 hour 2.5 mM $^{13}\text{C}_5$ glutamine treatment in glutamine-free DMEM/F12 medium. The cells were washed with 75 mM ammonium bicarbonate buffer (pH 7.4) and snap-frozen in liquid nitrogen for metabolite extraction.

For the extraction of metabolites from primary rib cage chondrocytes, an extraction buffer containing methanol:acetonitrile:water (40:40:20, v/v/v) along with internal standards ($\text{U}^{13}\text{C}^{15}\text{N}$ -amino acids, $^{13}\text{C}_{10}$ -ATP, $^{13}\text{C}_{10}$ - $^{15}\text{N}_5$ -AMP, $^{15}\text{N}_5$ -ADP, and citric acid D_4) was added. The mixture was incubated for 20 min at -20°C . Following incubation, the wells were repeatedly washed with extraction buffer to ensure complete lysis and harvest of cells/material. To promote cell lysis, cell lysates were frozen and thawed before centrifugation at 4°C, 21,000g. The supernatant was carefully transferred to remove any cellular debris, while the pellet was used for protein quantification. The supernatant was then dried in a SpeedVac concentrator set to 20°C at 1000 rpm until complete dryness.

Anion-exchange chromatography triple quadrupole mass spectrometry for the analysis of TCA cycle metabolites from femur head tissue

The dried pellet of the metabolite extract was resuspended in 150 μ l of UPLC-grade water (VWR) and transferred to 2-ml glass vials with 200 μ l inserts (CZT). These vials were placed in a precooled auto sampler 6°C of the ion chromatography system (ICS 5000+,

Thermo Fisher Scientific). The used protocol was adopted from a previously published method (61).

In brief, 10 μ l of the resuspended metabolite extract were injected, using full-loop mode with an overflow factor of 3, onto a Dionex IonPac AS11-HC column (2 mm by 250 mm, 4- μ m particle size, Thermo Fisher Scientific) equipped with a Dionex IonPac AG11-HC guard column (2 mm by 50 mm, 4 μ m, Thermo Fisher Scientific), which was held at a temperature of 30°C. Compound were eluted from the column using a potassium hydroxide gradient, which was generated by the eluent generator deionized water (Merck Millipore). The metabolite separation was carried out at a flow rate of 380 μ l/min, applying the following gradient: 0 to 5 min, 10 to 25 mM KOH; 5 to 21 min, 25 to 35 mM KOH; 21 to 25 min, 35 to 100 mM KOH; 25 to 28 min, 100 mM KOH; 28 to 32 min; 100 to 10 mM KOH. The column was reequilibrated at 10 mM for 6 min before ejecting the subsequent sample.

The eluting metabolites were detected in negative ion mode using ESI multi reaction monitoring on a Xevo TQ triple quadrupole mass spectrometer (Waters) applying the following electronic and gas settings: capillary voltage 1.5 kV, desolvation temperature 550°C, desolvation gas flow 800 liter/hour, and collision cell gas flow 0.15 ml/min. For the analysis of the targeted metabolites, two transitions were measured (qualifier and quantifier). The used transition and settings used for the relative quantification were pyruvic acid: mass/charge ratio (m/z) precursor mass (M-H+) 87, fragment mass (M-H+) m/z 59, used cone voltage 20 V, used collision energy 8 V; lactic acid: m/z precursor mass (M-H+) 90, fragment mass (M-H+) m/z 43, used cone voltage 26 V, used collision energy 12 V; citric acid: m/z precursor mass (M-H+) 191, fragment mass (M-H+) m/z 111, used cone voltage 18 V, used collision energy 10 V; aconitic acid: m/z precursor mass (M-H+) 173, fragment mass (M-H+) m/z 85, used cone voltage 16 V, used collision energy 12 V; isocitric acid: m/z precursor mass (M-H+) 191, fragment mass (M-H+) m/z 111, used cone voltage 18 V, used collision energy 12 V; α -ketoglutaric acid: m/z precursor mass (M-H+) 145, fragment mass (M-H+) m/z 56 used cone voltage 18 V, used collision energy 12 V; succinic acid: precursor mass (M-H+) 117, fragment mass (M-H+) m/z 55, used cone voltage 20 V, used collision energy 14 V; fumaric acid: precursor mass (M-H+) 115, fragment mass (M-H+) m/z 27, used cone voltage 22 V, used collision energy 8 V; and malic acid: precursor mass (M-H+) 132, fragment mass (M-H+) m/z 71, used cone voltage 22 V, used collision energy 16 V. Peak integration and subsequent data analysis were performed using the TargetLynx software (Waters).

Anion-exchange chromatography high-resolution mass spectrometry for the analysis of TCA cycle metabolites from primary rib cage chondrocytes

Similar to the targeted analysis of TCA cycle intermediates, the analysis of rib cage chondrocytes was performed on a Thermo Fisher Scientific anion-exchange system. However, instead of the above described ICS5000+ system, an Integriion system was used. Parameters and chromatographic columns were identical. The parameters for the HRMS analysis were the following: spray voltage 3.2 kV, capillary temperature was set to 300°C, sheath gas flow 50 arbitrary units (AU), aux gas flow 20 AU at a temperature of 330°C, and a sweep gas flow of 2 AU. The S-lens was set to a value of 50.

LC-MS-based analysis of steady-state and ^{13}C -traced amino acids

Amino acid analysis was performed according to an adopted benzoyl chloride derivatization protocol from the Kennedy laboratory (62, 63). For this purpose, the dried metabolite pellet was resuspended in 50 μ l of UPLC-grade water (VWR) and transferred to 2-ml glass vials with 200- μ l inserts (CZT). In the first step, 25 μ l of 100 mM sodium carbonate (Sigma-Aldrich) were added, followed by the addition of 25 μ l of 2% benzoyl chloride (Sigma-Aldrich) in UPLC-grade acetonitrile (VWR). The samples were placed in an Acquity iClass UPLC (Waters) sample manager at 20°C connected to a Q-Exactive (QE)-HF high-resolution accurate mass orbitrap-type mass spectrometer (Thermo Fisher Scientific).

For the analysis, 2 μ l of the derivatized sample were injected onto a 100 mm-by-1.0 mm HSS T3 column, packed with 1.8- μ m particles (Waters). The flow rate was 100 μ l/min, and the buffer system consisted of buffer A (10 mM ammonium formate, 0.15% formic acid in water) and buffer B (acetonitrile). The gradient was, as described in Wong *et al.* (62, 63): 0% B at 0 min; 0 to 15% B 0 to 0.1 min; 15 to 17% B 0.1 to 0.5 min; 17 to 55% B 0.5 to 14 min; 55 to 70% B 14 to 14.5 min; 70 to 100% B 14.5 to 18 min; 100% B 18 to 19 min; 100 to 0% B 19 to 19.1 min, 19.1 to 28 min 0% B.

The QE-HF mass spectrometer was operating in positive ionization mode monitoring in the mass range m/z 50 to 750. The applied resolution was 60,000, with an acquired gain control ion target of 3E6 and a maximal ion time of 100 ms. The heated ESI source was operating with a spray voltage of 3.5 kV, a capillary temperature of 250°C, a sheath gas flow of 60 AU, and an auxiliary gas flow of 20 AU at a temperature of 250°C. The S-lens was set to 60. Data analysis was performed using TraceFinder 4.1 (Thermo Fisher Scientific) targeting the derivatized proteinogenic amino acids as described previously (62, 63).

LC-HRMS data analysis

The LC-MS data analysis of the amine and the TCA compounds was performed using the TraceFinder software (version 5.1, Thermo Fisher Scientific). The identity of each compound was validated by authentic reference compounds, which were measured at the beginning and the end of the sequence. For data analysis the area of all detectable isotopologs mass peaks of every required compound were extracted and integrated using a mass accuracy <3 parts per million and a retention time tolerance of <0.05 min as compared to the independently measured reference compounds. If no independent ^{12}C experiments were carried out, where the pool size was determined from the obtained peak area of the ^{12}C monoisotopolog, the pool size determination was carried out by summing up the peak areas of all detectable isotopologs per compound. These areas were then normalized, as performed for untraced ^{12}C experiments, to the internal standards, which were added to the extraction buffer, followed by a normalization to the fresh weight of the analyzed samples. The relative isotope distribution of each isotopolog was calculated from the proportion of the peak area of each isotopolog toward the sum of all detectable isotopologs. Calculations and corrections for natural isotope abundance were performed using the AccuCor R-package (64).

Electron microscopy

Isolated P28 femur head cartilage was directly fixed in 2.5% glutaraldehyde (Serva) for 24 hours at 4°C. After fixation, the tissue was

cooled on ice and subjected to multiple steps including incubation with 0.1 M Sörensen's phosphate buffer (0.1 M KH_2PO_4) two times for 30 min, 2% osmium tetroxide (Sigma-Aldrich) incubation for 2 hours, and again 0.1 M Sörensen's phosphate buffer two times for 30 min. Moreover, the tissue was incubated in an ethanol gradient from 30, 40, 50, to 60% for 30 min each. Afterward, 1% uranyl acetate diluted in 70% EtOH was applied for 1 hour. Afterward, ethanol gradient was conducted from 70, 80, 90, 95, to 100% for 30 min each. Last, the samples were removed from ice and followed by EPON embedding according to the manufacturer's instructions (Sigma-Aldrich). Therefore, the samples were preincubated in propyl enoxide two times for 30 min and afterward subjected to propyl enoxide-EPON (3:1) for 5 hours. This solution was exchanged to propyl enoxide-EPON (1:1) mixture for overnight incubation. Last, the tissue was embedded in EPON and polymerized for 2 days before microscopy. To evaluate the ultrastructure, the samples were cut in ultrathin sections and analyzed by transmission electron microscopy in a blinded manner (LEO 906E; Oberkochen).

Flow cytometry

Primary isolated ribcage chondrocytes were precultured in standard growth medium (DMEM/F12, 10% FCS, 1% P/S, and ASC) for 24 hours before amino acid starvation for 3 days. Apoptosis was detected as previously described (24). Specifically, cell culture medium and collagenase-dissociated chondrocytes were combined and subjected to sequential washes in PBS and AnxA5-binding buffer (10 mM Hepes, 140 mM NaCl, and 2.5 mM CaCl_2 (pH 7.4)). Chondrocytes were stained with AnxA5-Cy2 (1:100, Immundiagnostik, AP1011AG) and SYTOX Blue Dead Cell Stain (1:200, Life Technologies, S34857) in 50 μl of AnxA5-binding buffer for 15 min at RT in the absence of light, diluted with 150 μl of AnxA5-binding buffer, and stored on ice until cellular fluorescence was quantified using a BD FACS Canto II instrument. A uniform cell population was gated in the FSC/SSC plot, and within this population, the proportion of AnxA5⁺ and AnxA5⁺/SytoxBlue⁺ cells were quantified as percentage of cell death.

Declaration of generative AI and AI-assisted technologies in the writing process

During the preparation of this work, the author used Chat GPT-4 (non-turbo) to improve language and readability. After using this tool/service, the author reviewed and edited the content as needed and takes full responsibility for the content of the publication. The following prompts were used: Conciseness & Clarity: You often ask for shortening or rephrasing while keeping the meaning intact. Formal & Precise Wording: You prefer avoiding overly enthusiastic language in professional communication. Avoiding Specific Words: Sometimes, you request alternatives for words like "moreover" or "appreciate." Scientific & Technical Accuracy: Your edits often refine explanations in manuscripts related to ECM, cartilage, and mitochondrial function. Grammar & Flow: You want smooth, well-structured sentences, avoiding redundancy.

Statistical analysis

All relevant information on the statistical details of experiments is provided in the figure legends. To determine statistical significance between two groups, the unpaired two-tailed Student's *t* test was used, and to compare multiple groups, one-way analysis of variance (ANOVA) with Bonferroni's multiple comparisons test was conducted using GraphPad Prism. Individual mean values \pm SEM are

presented. Significance was calculated for $n \geq 3$ and is given in the figure legends. * $P < 0.05$, ** $P < 0.01$, *** $P < 0.001$.

Supplementary Materials

This PDF file includes:

Supplementary Materials and Methods

Figs. S1 to S9

Table S1

REFERENCES AND NOTES

- G. S. Gorman, P. F. Chinnery, S. DiMauro, M. Hirano, Y. Koga, R. McFarland, A. Suomalainen, D. R. Thorburn, M. Zeviani, D. M. Turnbull, Mitochondrial diseases. *Nat. Rev. Dis. Primers* **2**, 16080 (2016).
- E. Fernandez-Zizarra, M. Zeviani, Mitochondrial disorders of the OXPHOS system. *FEBS Lett.* **595**, 1062–1106 (2021).
- M. K. Koenig, Presentation and diagnosis of mitochondrial disorders in children. *Pediatr. Neurol.* **38**, 305–313 (2008).
- G. Sturm, K. R. Karan, A. S. Monzel, B. Santhanam, T. Taivassalo, C. Bris, S. A. Ware, M. Cross, A. Towheed, A. Higgins-Chen, M. J. McManus, A. Cardenas, J. Lin, E. S. Epel, S. Rahman, J. Vissing, B. Grassi, M. Levine, S. Horvath, R. G. Haller, G. Lenaers, D. C. Wallace, M. P. St-Onge, S. Tavazoie, V. Procaccio, B. A. Kaufman, E. L. Seifert, M. Hirano, M. Picard, OxPhos defects cause hypermetabolism and reduce lifespan in cells and in patients with mitochondrial diseases. *Commun. Biol.* **6**, 22 (2023).
- R. L. Boal, Y. S. Ng, S. J. Pickett, A. M. Schaefer, C. Feeney, A. Bright, R. W. Taylor, D. M. Turnbull, G. S. Gorman, T. Cheetham, R. McFarland, Height as a clinical biomarker of disease burden in adult mitochondrial disease. *J. Clin. Endocrinol. Metab.* **104**, 2057–2066 (2019).
- T. Holzer, K. Probst, J. Etich, M. Auler, V. S. Georgieva, B. Bluhm, C. Frie, J. Heilig, A. Niehoff, J. Nuchel, M. Plomann, J. M. Seeger, H. Kashkar, O. R. Baris, R. J. Wiesner, B. Brachvogel, Respiratory chain inactivation links cartilage-mediated growth retardation to mitochondrial diseases. *J. Cell Biol.* **218**, 1853–1870 (2019).
- A. E. Borjesson, S. H. Windahl, E. Karimian, E. E. Eriksson, M. K. Lagerquist, C. Engdahl, M. C. Antal, A. Krust, P. Chambon, L. Savendahl, C. Ohlsson, The role of estrogen receptor- α and its activation function-1 for growth plate closure in female mice. *Am. J. Physiol. Endocrinol. Metab.* **302**, E1381–E1389 (2012).
- K. Bubb, T. Holzer, J. L. Nolte, M. Kruger, R. Wilson, U. Schlotzer-Schrehardt, J. Brinckmann, J. Altmüller, A. Aszodi, L. Fleischhauer, H. Clausen-Schaumann, K. Probst, B. Brachvogel, Mitochondrial respiratory chain function promotes extracellular matrix integrity in cartilage. *J. Biol. Chem.* **297**, 101224 (2021).
- P. K. Arnold, L. W. S. Finley, Regulation and function of the mammalian tricarboxylic acid cycle. *J. Biol. Chem.* **299**, 102838 (2023).
- S.-M. Fendt, E. L. Bell, M. A. Keibler, B. A. Olenchok, J. R. Mayers, T. M. Wasylenko, N. I. Vokes, L. Guarente, M. G. Vander Heiden, G. Stephanopoulos, Reductive glutamine metabolism is a function of the alpha-ketoglutarate to citrate ratio in cells. *Nat. Commun.* **4**, 2236 (2013).
- O. E. Owen, S. C. Kalhan, R. W. Hanson, The key role of anaplerosis and cataplerosis for citric acid cycle function. *J. Biol. Chem.* **277**, 30409–30412 (2002).
- K. J. Humphrey, O. Karayel, D. E. James, M. Mann, High-throughput and high-sensitivity phosphoproteomics with the EasyPhos platform. *Nat. Protoc.* **13**, 1897–1916 (2018).
- R. Ke, Q. Xu, C. Li, L. Luo, D. Huang, Mechanisms of AMPK in the maintenance of ATP balance during energy metabolism. *Cell Biol. Int.* **42**, 384–392 (2018).
- J. L. Van Nostrand, K. Hellberg, E.-C. Luo, E. L. Van Nostrand, A. Dayn, J. Yu, M. N. Shokhirev, Y. Dayn, G. W. Yeo, R. J. Shaw, AMPK regulation of Raptor and TSC2 mediate metformin effects on transcriptional control of anabolism and inflammation. *Genes Dev.* **34**, 1330–1344 (2020).
- A. Yanagijya, E. Suyama, H. Adachi, Y. V. Svitkin, P. Aza-Blanc, H. Imataka, S. Mikami, Y. Martineau, Z. A. Ronai, N. Sonenberg, Translational homeostasis via the mRNA cap-binding protein, eIF4E. *Mol. Cell* **46**, 847–858 (2012).
- S. A. Fernandes, D.-D. Angelidakis, J. Nuchel, J. Pan, P. Gollwitzer, Y. Elkis, F. Artoni, S. Wilhelm, M. Kovacevic-Sarmiento, C. Demetriades, Spatial and functional separation of mTORC1 signalling in response to different amino acid sources. *Nat. Cell Biol.* **26**, 1918–1933 (2024).
- R. A. Saxton, D. M. Sabatini, mTOR signaling in growth, metabolism, and disease. *Cell* **168**, 960–976 (2017).
- V. Ravi, A. Jain, S. Mishra, N. R. Sundaresan, Measuring protein synthesis in cultured cells and mouse tissues using the non-radioactive SUNSET assay. *Curr. Protoc. Mol. Biol.* **133**, e127 (2020).
- G. Li, D. Li, T. Wang, S. He, Pyrimidine biosynthetic enzyme CAD: Its function, regulation, and diagnostic potential. *Int. J. Mol. Sci.* **22**, (2021).

20. H. Yoo, M. R. Antoniewicz, G. Stephanopoulos, J. K. Kelleher, Quantifying reductive carboxylation flux of glutamine to lipid in a brown adipocyte cell line. *J. Biol. Chem.* **283**, 20621–20627 (2008).
21. Y. Rabanal-Ruiz, E. G. Otten, V. I. Korolchuk, mTORC1 as the main gateway to autophagy. *Essays Biochem.* **61**, 565–584 (2017).
22. X. Kang, W. Yang, D. Feng, X. Jin, Z. Ma, Z. Qian, T. Xie, H. Li, J. Liu, R. Wang, F. Li, D. Li, H. Sun, S. Wu, Cartilage-specific autophagy deficiency promotes ER stress and impairs chondrogenesis in PERK-ATF4-CHOP-dependent manner. *J. Bone Miner. Res.* **32**, 2128–2141 (2017).
23. C. Demetriades, N. Doumpas, A. A. Teleman, Regulation of TORC1 in response to amino acid starvation via lysosomal recruitment of TSC2. *Cell* **156**, 786–799 (2014).
24. S. Rosenbaum, S. Kreft, J. Etich, C. Frie, J. Stermann, I. Grskovic, B. Frey, D. Mielenz, E. Pöschl, U. Gaipf, M. Paulsson, B. Brachvogel, Identification of novel binding partners (annexins) for the cell death signal phosphatidylserine and definition of their recognition motif. *J. Biol. Chem.* **286**, 5708–5716 (2011).
25. J. Yoshino, J. A. Baur, S. I. Imai, NAD⁺ intermediates: The biology and therapeutic potential of NMN and NR. *Cell Metab.* **27**, 513–528 (2018).
26. Z. Chen, B. Bordieanu, R. Kesavan, N. P. Lesner, S. S. K. Venigalla, S. D. Shelton, R. J. DeBerardinis, P. Mishra, Lactate metabolism is essential in early-onset mitochondrial myopathy. *Sci. Adv.* **9**, eadd3216 (2023).
27. D. Weiland, B. Brachvogel, H.-T. Hornig-Do, J. F. G. Neuhaus, T. Holzer, D. J. Tobin, C. M. Niessen, R. J. Wiesner, O. R. Baris, Imbalance of mitochondrial respiratory chain complexes in the epidermis induces severe skin inflammation. *J. Invest. Dermatol.* **138**, 132–140 (2018).
28. R. M. Denton, P. J. Randle, B. J. Bridges, R. H. Cooper, A. L. Kerbey, H. T. Pask, D. L. Severson, D. Stansbie, S. Whitehouse, Regulation of mammalian pyruvate dehydrogenase. *Mol. Cell. Biochem.* **9**, 27–53 (1975).
29. P. J. Randle, E. A. Newsholme, P. B. Garland, Regulation of glucose uptake by muscle. 8. Effects of fatty acids, ketone bodies and pyruvate, and of alloxan-diabetes and starvation, on the uptake and metabolic fate of glucose in rat heart and diaphragm muscles. *Biochem. J.* **93**, 652–665 (1964).
30. P. B. Garland, P. J. Randle, Regulation of glucose uptake by muscles. 10. Effects of alloxan-diabetes, starvation, hypophysectomy and adrenalectomy, and of fatty acids, ketone bodies and pyruvate, on the glycerol output and concentrations of free fatty acids, long-chain fatty acyl-coenzyme A, glycerol phosphate and citrate-cycle intermediates in rat heart and diaphragm muscles. *Biochem. J.* **93**, 678–687 (1964).
31. P. B. Garland, E. A. Newsholme, P. J. Randle, Regulation of glucose uptake by muscle. 9. Effects of fatty acids and ketone bodies, and of alloxan-diabetes and starvation, on pyruvate metabolism and on lactate-pyruvate and L-glycerol 3-phosphate-dihydroxyacetone phosphate concentration ratios in rat heart and rat diaphragm muscles. *Biochem. J.* **93**, 665–678 (1964).
32. A. R. Mullen, W. W. Wheaton, E. S. Jin, P. H. Chen, L. B. Sullivan, T. Cheng, Y. Yang, W. M. Linehan, N. S. Chandel, R. J. DeBerardinis, Reductive carboxylation supports growth in tumour cells with defective mitochondria. *Nature* **481**, 385–388 (2011).
33. J. B. Spinelli, P. C. Rosen, H. G. Sprenger, A. M. Puszynska, J. L. Mann, J. M. Roessler, A. L. Cangelosi, A. Henne, K. J. Condon, T. Zhang, T. Kunchok, C. A. Lewis, N. S. Chandel, D. M. Sabatini, Fumarate is a terminal electron acceptor in the mammalian electron transport chain. *Science* **374**, 1227–1237 (2021).
34. P. Altea-Manzano, A. Vandekeere, J. Edwards-Hicks, M. Roldan, E. Abraham, X. Lleshi, A. N. Guerrieri, D. Berardi, J. Wills, J. M. Junior, A. Pantazi, J. C. Acosta, R. M. Sanchez-Martin, S. M. Fendt, M. Martin-Hernandez, A. J. Finch, Reversal of mitochondrial malate dehydrogenase 2 enables anaplerosis via redox rescue in respiration-deficient cells. *Mol. Cell* **82**, 4537–4547.e7 (2022).
35. V. I. Bunik, A. R. Fernie, Metabolic control exerted by the 2-oxoglutarate dehydrogenase reaction: A cross-kingdom comparison of the crossroad between energy production and nitrogen assimilation. *Biochem. J.* **422**, 405–421 (2009).
36. S. Stegen, G. Rinaldi, S. Loopmans, I. Stockmans, K. Moermans, B. Thienpont, S. M. Fendt, P. Carmeliet, G. Carmeliet, Glutamine metabolism controls chondrocyte identity and function. *Dev. Cell* **53**, 530–544.e8 (2020).
37. K. Birsoy, T. Wang, W. W. Chen, E. Freinkman, M. Abu-Remaileh, D. M. Sabatini, An essential role of the mitochondrial electron transport chain in cell proliferation is to enable aspartate synthesis. *Cell* **162**, 540–551 (2015).
38. K. E. R. Hollinshead, H. Munford, K. L. Eales, C. Bardella, C. Li, C. Escibano-Gonzalez, A. Thakker, Y. Nonnenmacher, K. Kluckova, M. Jeeves, R. Murren, F. Cuozzo, D. Ye, G. Laurenti, W. Zhu, K. Hiller, D. J. Hodson, W. Hua, I. P. Tomlinson, C. Ludwig, Y. Mao, D. A. Tennant, Oncogenic IDH1 mutations promote enhanced proline synthesis through PYCR1 to support the maintenance of mitochondrial redox homeostasis. *Cell Rep.* **22**, 3107–3114 (2018).
39. H. Hoitzing, P. A. Gammage, L. V. Haute, M. Minczuk, I. G. Johnston, N. S. Jones, Energetic costs of cellular and therapeutic control of stochastic mitochondrial DNA populations. *PLoS Comput. Biol.* **15**, e1007023 (2019).
40. V. I. Korolchuk, A. Mansilla, F. M. Menzies, D. C. Rubinsztein, Autophagy inhibition compromises degradation of ubiquitin-proteasome pathway substrates. *Mol. Cell* **33**, 517–527 (2009).
41. A. G. Hinnebusch, Translational homeostasis via eIF4E and 4E-BP1. *Mol. Cell* **46**, 717–719 (2012).
42. A. Efeyan, R. Zoncu, S. Chang, I. Gumper, H. Snitkin, R. L. Wolfson, O. Kirak, D. D. Sabatini, D. M. Sabatini, Regulation of mTORC1 by the Rag GTPases is necessary for neonatal autophagy and survival. *Nature* **493**, 679–683 (2013).
43. A. A. Bielska, C. F. Harrigan, Y. J. Kyung, Q. Morris, W. Palm, C. B. Thompson, Activating mTOR mutations are detrimental in nutrient-poor conditions. *Cancer Res.* **82**, 3263–3274 (2022).
44. G. Leprévier, M. Remke, B. Rotblat, A. Dubuc, A. R. Mateo, M. Kool, S. Agnihotri, A. El-Naggar, B. Yu, S. P. Somasekharan, B. Faubert, G. Bridon, C. E. Tognon, J. Mathers, R. Thomas, A. Li, A. Barokas, B. Kwok, M. Bowden, S. Smith, X. Wu, A. Korshunov, T. Hielscher, P. A. Northcott, J. D. Galpin, C. A. Ahern, Y. Wang, M. G. McCabe, V. P. Collins, R. G. Jones, M. Pollak, O. Delattre, M. E. Gleave, E. Jan, S. M. Pfister, C. G. Proud, W. B. Derry, M. D. Taylor, P. H. Sorensen, The eEF2 kinase confers resistance to nutrient deprivation by blocking translation elongation. *Cell* **153**, 1064–1079 (2013).
45. A. A. Teleman, Y.-W. Chen, S. M. Cohen, 4E-BP functions as a metabolic brake used under stress conditions but not during normal growth. *Genes Dev.* **19**, 1844–1848 (2005).
46. E. Kim, P. Goraksha-Hicks, L. Li, T. P. Neufeld, K. L. Guan, Regulation of TORC1 by Rag GTPases in nutrient response. *Nat. Cell Biol.* **10**, 935–945 (2008).
47. N. A. Khan, M. Auranen, I. Paetau, E. Pirinen, L. Euro, S. Forsstrom, L. Pasila, V. Velagapudi, C. J. Carroll, J. Auwerx, A. Suomalainen, Effective treatment of mitochondrial myopathy by nicotinamide riboside, a vitamin B3. *EMBO Mol. Med.* **6**, 721–731 (2014).
48. J. M. Hollander, L. Li, M. Rawal, S. K. Wang, Y. Shu, M. Zhang, H. C. Nielsen, C. J. Rosen, L. Zeng, A critical bioenergetic switch is regulated by IGF2 during murine cartilage development. *Commun. Biol.* **5**, 1230 (2022).
49. C. Moschandrea, V. Kondylis, I. Evangelakos, M. Herholz, F. Schneider, C. Schmidt, M. Yang, S. Ehret, M. Heine, M. Y. Jaekstein, K. Szczepanowska, R. Schwarzer, L. Baumann, T. Bock, E. Nikitopoulou, S. Brodessa, M. Kruger, C. Frezza, J. Heeren, A. Trifunovic, M. Pasparakis, Mitochondrial dysfunction abrogates dietary lipid processing in enterocytes. *Nature* **625**, 385–392 (2024).
50. S. J. Ricout, B. D. Manning, The multifaceted role of mTORC1 in the control of lipid metabolism. *EMBO Rep.* **14**, 242–251 (2013).
51. C. M. Deus, K. F. Yambire, P. J. Oliveira, N. Raimundo, Mitochondria-lysosome crosstalk: From physiology to neurodegeneration. *Trends Mol. Med.* **26**, 71–88 (2020).
52. L. Fernández-Mosquera, C. V. Diogo, K. F. Yambire, G. L. Santos, M. Luna Sánchez, P. Benit, P. Rustin, L. C. Lopez, I. Milosevic, N. Raimundo, Acute and chronic mitochondrial respiratory chain deficiency differentially regulate lysosomal biogenesis. *Sci. Rep.* **7**, 45076 (2017).
53. M. Graef, J. Nunnari, Mitochondria regulate autophagy by conserved signalling pathways. *EMBO J.* **30**, 2101–2114 (2011).
54. H. E. Thomas, Y. Zhang, J. A. Stefely, S. R. Veiga, G. Thomas, S. C. Kozma, C. A. Mercer, Mitochondrial complex I activity is required for maximal autophagy. *Cell Rep.* **24**, 2404–2417.e8 (2018).
55. B. Yan, Z. Zhang, D. Jin, C. Cai, C. Jia, W. Liu, T. Wang, S. Li, H. Zhang, B. Huang, P. Lai, H. Wang, A. Liu, C. Zeng, D. Cai, Y. Jiang, X. Bai, mTORC1 regulates PTHrP to coordinate chondrocyte growth, proliferation and differentiation. *Nat. Commun.* **7**, 11151 (2016).
56. D. A. Ovchinnikov, J. M. Deng, G. Ogunrinu, R. R. Behringer, Col2a1-directed expression of Cre recombinase in differentiating chondrocytes in transgenic mice. *Genesis* **26**, 145–146 (2000).
57. V. Kumar, J. E. Bouameur, J. Bär, R. H. Rice, H. T. Hornig-Do, D. R. Roop, N. Schwarz, S. Brodessa, S. Thiering, R. E. Leube, R. J. Wiesner, P. Vijayaraj, C. B. Brazel, S. Heller, H. Binder, H. Löffler-Wirth, P. Seibel, T. M. Magin, A keratin scaffold regulates epidermal barrier formation, mitochondrial lipid composition, and activity. *J. Cell Biol.* **211**, 1057–1075 (2015).
58. C. Özbalci, T. Sachsenheimer, B. Brügger, Quantitative analysis of cellular lipids by nano-electrospray ionization mass spectrometry. *Methods Mol. Biol.* **1033**, 3–20 (2013).
59. S. M. Turpin-Nolan, P. Hammerschmidt, W. Chen, A. Jais, K. Timper, M. Awazawa, S. Brodessa, J. C. Brüning, CerS1-derived C_{18:0} ceramide in skeletal muscle promotes obesity-induced insulin resistance. *Cell Rep.* **26**, 1–10.e7 (2019).
60. M. W. Pfaffl, A new mathematical model for relative quantification in real-time RT-PCR. *Nucleic Acids Res.* **29**, e45 (2001).
61. M. Schwaiger, E. Rampler, G. Hermann, W. Miklos, W. Berger, G. Koellensperger, Anion-exchange chromatography coupled to high-resolution mass spectrometry: A powerful tool for merging targeted and non-targeted metabolomics. *Anal. Chem.* **89**, 7667–7674 (2017).
62. P. A. Malec, M. Oteri, V. Inferra, F. Cacciola, L. Mondello, R. T. Kennedy, Determination of amines and phenolic acids in wine with benzoyl chloride derivatization and liquid chromatography-mass spectrometry. *J. Chromatogr. A* **1523**, 248–256 (2017).

63. J. M. Wong, P. A. Malec, O. S. Mabrouk, J. Ro, M. Dus, R. T. Kennedy, Benzoyl chloride derivatization with liquid chromatography-mass spectrometry for targeted metabolomics of neurochemicals in biological samples. *J. Chromatogr. A* **1446**, 78–90 (2016).
64. X. Su, W. Lu, J. D. Rabinowitz, Metabolite spectral accuracy on orbitraps. *Anal. Chem.* **89**, 5940–5948 (2017).

Acknowledgments: We acknowledge the use of Chat GPT-4 (non-turbo) to improve language and readability. **Funding:** This work was supported by German Research Foundation grant (DFG) to the Research Unit FOR2722 BR2304/12-1 - 407146744 (B.B.) and BR2304/12-2 - 384170921 (B.B.), German Research Foundation grant (DFG) to the Research Unit FOR2722 ET144/3-2 - 384170921 (J.E.), German Research Foundation grant (DFG) to the Research Unit FOR2722 DE3170/1-1 - 384170921 (C.D.), German Research Foundation grant (DFG) to the Research Unit FOR2722 KR3788/8-2 - 384170921 (M.K.), German Research Foundation grant (DFG) to the Research Unit FOR2722 NU467/1-1 - 384170921 (J.N.), and German Research Foundation grant (DFG) BR2304/7-1 - 207342459 (B.B.). **Author contributions:** Conceptualization: K.B., J.E., C.D., P.G., J.R., and B.B. Methodology: K.B., J.E., J.L.N., M.K., C.D., and P.G. Validation: K.B., J.E., K.P., T.P., M.S., S.R., M.K., U.S.-S., J.N., P.G., and B.B. Formal analysis: K.B.,

J.E., K.P., M.S., F.D., J.L.N., M.K., P.G., and B.B. Investigation: K.B., J.E., K.P., T.P., M.S., S.R., M.K., U.S.-S., J.N., and P.G. Resources: F.D., M.K., C.D., P.G., and B.B. Data curation: K.B., J.E., M.S., M.K., P.G., and B.B. Writing—original draft: K.B. and B.B. Review and editing: K.B., J.E., K.P., T.P., F.D., M.K., U.S.-S., J.N., C.D., P.G., J.R., and B.B. Visualization: K.B., J.E., K.P., T.P., M.K., P.G., and B.B. Supervision: J.R., M.S., C.D., P.G., and B.B. Project administration: C.D. and B.B. Funding acquisition: J.E., M.K., J.N., C.D., and B.B. **Competing interests:** The authors declare that they have no competing interests. **Data and materials availability:** All data needed to evaluate the conclusions in the paper are present in the paper and/or the Supplementary Materials. In addition, mass spectrometry data from proteome analysis have been deposited to the ProteomeXchange Consortium via the PRIDE partner repository with the dataset identifier PXD027109 and are publicly available. The metabolome dataset has been deposited at Zenodo under the DOI 10.5281/zenodo.8431026. This paper does not report original code.

Submitted 2 August 2024

Accepted 14 March 2025

Published 18 April 2025

10.1126/sciadv.ads1842